Monthly Notices
of the
ROYAL ASTRONOMICAL SOCIETY

Mon. Not. R. Astron. Soc. **418,** 1649–1667 (2011) doi:10.1111/j.1365-2966.2011.19583.x

Cosmic evolution of the atomic and molecular gas contents of galaxies

Claudia del P. Lagos,[1⋆] Carlton M. Baugh,[1] Cedric G. Lacey,[1] Andrew J. Benson,[2] Han-Seek Kim[3] and Chris Power[4,5]

[1]*Department of Physics, Institute for Computational Cosmology, University of Durham, South Road, Durham DH1 3LE*
[2]*California Institute of Technology, Pasadena, CA 91125, USA*
[3]*School of Physics, University of Melbourne, Parkville, VIC 3010, Australia*
[4]*Department of Physics & Astronomy, University of Leicester, Leicester LE1 7RH*
[5]*Astronomy and Astrophysics Department, The University of Western Australia, 35 Stirling Highway, Crawley, WA 6009, Australia*

Accepted 2011 August 3. Received 2011 July 27; in original form 2011 May 10

ABSTRACT

We study the evolution of the cold gas content of galaxies by splitting the interstellar medium into its atomic and molecular hydrogen components, using the galaxy formation model GALFORM in the Λ cold dark matter framework. We calculate the molecular-to-atomic hydrogen mass ratio, H_2/H I, in each galaxy using two different approaches, the pressure-based empirical relation of Blitz & Rosolowsky and the theoretical model of Krumholz, McKeee & Tumlinson, and apply them to consistently calculate the star formation rates of galaxies. We find that the model based on the Blitz & Rosolowsky law predicts an H I mass function, ^{12}CO (1–0) luminosity function, correlations between H_2/H I and stellar and cold gas mass, and infrared–^{12}CO molecule luminosity relation in good agreement with local and high-redshift observations. The H I mass function evolves weakly with redshift, with the number density of high-mass galaxies decreasing with increasing redshift. In the case of the H_2 mass function, the number density of massive galaxies increases strongly from $z = 0$ to 2, followed by weak evolution up to $z = 4$. We also find that H_2/H I of galaxies is strongly dependent on stellar and cold gas mass, and also on redshift. The slopes of the correlations between H_2/H I and stellar and cold gas mass hardly evolve, but the normalization increases by up to two orders of magnitude from $z = 0$ to 8. The strong evolution in the H_2 mass function and H_2/H I is primarily due to the evolution in the sizes of galaxies and, secondarily, in the gas fractions. The predicted cosmic density evolution of H I agrees with the observed evolution inferred from damped Lyα systems, and is always dominated by the H I content of low- and intermediate-mass haloes. We find that previous theoretical studies have largely overestimated the redshift evolution of the global H_2/H I due to limited resolution. We predict a maximum of $\rho_{H_2}/\rho_{H\,I} \approx 1.2$ at $z \approx 3.5$.

Key words: stars: formation – galaxies: evolution – galaxies: formation – galaxies: ISM.

1 INTRODUCTION

Star formation (SF) is a key process in galaxy formation and evolution. A proper understanding of SF and the mechanisms regulating it are necessary to reliably predict galaxy evolution. In recent years, there has been a growing interest in modelling SF with subgrid physics in cosmological scenarios, in which an accurate description of the interstellar medium (ISM) of galaxies is needed (e.g. Springel & Hernquist 2003; Schaye 2004; Narayanan et al. 2009; Cook et al. 2010; Dutton, van den Bosch & Dekel 2010; Fu et al. 2010; Schaye et al. 2010; Lagos et al. 2011, hereinafter L11).

It has been shown observationally that SF takes place in molecular clouds (see Solomon & Vanden Bout 2005, for a review). Moreover, the surface density of the star formation rate (SFR) correlates with the surface density of molecular hydrogen, H_2, in an approximately linear fashion, $\Sigma_{SFR} \propto \Sigma_{H_2}$ (e.g. Bigiel et al. 2008; Schruba et al. 2010). On the other hand, the correlation between Σ_{SFR} and the surface density of atomic hydrogen, H I, is much weaker. Low SFRs have been measured in low-stellar-mass, H I-dominated dwarfs and low-surface-brightness galaxies (e.g. Roychowdhury et al. 2009; Wyder et al. 2009), and larger SFRs in more massive galaxies with more abundant H_2, such as normal spiral and starburst galaxies (e.g. Kennicutt 1998; Wong & Blitz 2002).

Observational constraints on the H I and H_2 content of galaxies are now available for increasingly large samples. For H I, accurate

⋆E-mail: c.d.p.lagos@durham.ac.uk

measurements of the 21-cm emission in large surveys of local galaxies have been presented by Zwaan et al. (2005) using the H I Parkes All-Sky Survey (HIPASS; Meyer et al. 2004) and more recently by Martin et al. (2010) using the Arecibo Legacy Fast ALFA Survey (ALFALFA; Giovanelli et al. 2005). From these surveys, it has been possible to probe the H I mass function (MF) down to H I masses of $M_{\rm H\,I} \approx 10^6\,{\rm M}_\odot$ and to estimate the global H I mass density at $z = 0$, $\Omega_{\rm H\,I} = (3.6\text{–}4.2) \times 10^{-4}$ in units of the present-day critical density. These H I-selected galaxies are also characterized by weaker clustering (e.g. Basilakos et al. 2007; Meyer et al. 2007) than optically selected samples (e.g. Norberg et al. 2001), indicating that local H I-selected galaxies are preferentially found in lower mass haloes than their optical counterparts. At high redshift, information about H I is very limited since it is based mostly on absorption-line measurements in the spectra of quasi-stellar objects (QSOs; e.g. Péroux et al. 2003; Prochaska, Herbert-Fort & Wolfe 2005; Rao, Turnshek & Nestor 2006; Guimarães et al. 2009; Noterdaeme et al. 2009; see Rauch 1998 for a review of this technique). These observations suggest very little evolution of $\Omega_{\rm H\,I}$ up to $z \approx 5$. Intensity mapping of the 21-cm emission line is one of the most promising techniques to estimate H I mass abundances at high redshifts. This technique has recently been applied to estimate global H I densities at intermediate redshifts ($z \lesssim 0.8$), and has given estimates in agreement with the ones inferred from absorption-line measurements (e.g. Lah et al. 2007, 2009; Verheijen et al. 2007; Chang et al. 2010).

To study H_2, it is generally necessary to use emission from other molecules as tracers, since H_2 lacks a dipole moment, making emission from this molecule extremely weak and hard to detect in interstellar gas, which is typically cold. The most commonly used proxy for H_2 is the ^{12}CO molecule (hereinafter 'CO'), which is the second most abundant molecule in the Universe. Keres, Yun & Young (2003) reported the first attempt to derive the local luminosity function (LF) of CO (1–0) (the lowest energy transition of CO) from which they inferred the H_2 MF and the local $\Omega_{\rm H_2} = (1.1 \pm 0.4) \times 10^{-4}\,h^{-1}$, assuming a constant CO (1–0)–H_2 conversion factor. It has not yet been possible to estimate the cosmic H_2 abundance at high redshift. However, a few detections of H_2 absorption in the lines of sight to QSOs have been reported (e.g. Noterdaeme et al. 2008; Srianand et al. 2010; Tumlinson et al. 2010), as well as CO detections in a large number of luminous star-forming galaxies (e.g. Greve et al. 2005; Geach et al. 2009; Daddi et al. 2010; Tacconi et al. 2010).

Measurements of the H I and H_2 mass content, as well as other galaxy properties, are available in relatively large samples of local galaxies (running into a few hundreds), allowing the characterization of scaling relations between the cold gas and the stellar mass content. From these samples, it has been possible to determine that the molecular-to-atomic gas ratio correlates with stellar mass, and that there is an anticorrelation between the H I-to-stellar mass ratio and stellar mass (e.g. Bothwell, Kennicutt & Lee 2009; Catinella et al. 2010; Saintonge et al. 2011). However, these correlations exhibit large scatter and are either subject to biases in the construction of observational samples, such as inhomogeneity in the selection criteria, or sample a very narrow range of galaxy properties.

The observational constraints on H I and H_2 at higher redshifts will improve dramatically over the next decade with the next generation of radio and submillimetre telescopes such as the Australian SKA Pathfinder (ASKAP; Johnston et al. 2008), the Karoo Array Telescope (MeerKAT; Booth et al. 2009) and the Square Kilometre Array (SKA; Schilizzi, Dewdney & Lazio 2008) which aim to detect 21-cm emission from H I, and the Atacama Large Millimeter Array (ALMA; Wootten & Thompson 2009) and the Large Millimeter Telescope (LMT; Hughes et al. 2010) which are designed to detect emission from molecules. Here we investigate the predictions of galaxy formation models for the evolution of the H I and H_2 gas content of galaxies, taking advantage of the development of realistic SF models (e.g. Mac Low & Klessen 2004; Blitz & Rosolowsky 2006, hereinafter BR; Pelupessy, Papadopoulos & van der Werf 2006; Krumholz, McKee & Tumlinson 2009; Pelupessy & Papadopoulos 2009; see McKee & Ostriker 2007 for a review). In our approach, a successful model is one that, at the same time, reproduces the observed stellar masses, luminosities, morphologies and the atomic and molecular gas contents of galaxies at the present day. Using such a model, it is reasonable to extend the predictions to follow the evolution of the gas contents of galaxies towards high redshift.

Until recently, the ISM of galaxies in semi-analytic models was treated as a single star-forming phase (e.g. Cole et al. 2000; Springel et al. 2001; Cattaneo et al. 2008; Lagos, Cora & Padilla 2008; Somerville et al. 2008). The first attempts to predict the separate H I and H_2 contents of galaxies in semi-analytic models post-processed the output of single-phase ISM treatments to add this information a posteriori (e.g. Obreschkow et al. 2009a; Power, Baugh & Lacey 2010). It was only very recently that a proper fully self-consistent treatment of the ISM and SF in galaxies throughout the cosmological calculation was made (Cook et al. 2010; Fu et al. 2010; L11). We show in this work that this consistent treatment is necessary to make progress in understanding the gas contents of galaxies.

We use the semi-analytical model GALFORM (Cole et al. 2000) in a Λ cold dark matter (ΛCDM) cosmology with the improved treatment of SF implemented by L11, which explicitly splits the hydrogen content in the ISM of galaxies into H I and H_2. Our aims are (i) to study whether the models are able to predict H I and H_2 MFs in agreement with the observed ones at $z = 0$; (ii) to follow the evolution of the MFs towards high redshift; (iii) to compare with the observational results described above; and (iv) to study scaling relations of H_2/H I with galaxy properties. By doing so, it is possible to establish which physical processes are responsible for the evolution of H I and H_2 in galaxies.

This paper is organized as follows. In Section 2, we describe the main characteristics of the GALFORM model. In Section 3, we present local universe scaling relations and compare with available observations. In Section 4, we present the local H I and H_2 MFs, and the infrared (IR)–CO luminosity relation. We also investigate which galaxies dominate the H I and H_2 MFs and predict their evolution up to $z = 8$, and study the H I mass density measured in stacked samples of galaxies. In Section 5, we present predictions for the scaling relations of H_2/H I with galaxy properties and analyse the mechanisms underlying these relations. Section 6 presents the evolution of the cosmic densities of H I and H_2, and compares with observations. We also determine which range of halo mass dominates these densities. Finally, we discuss our results and present our conclusions in Section 7.

2 MODELLING THE TWO-PHASE COLD GAS IN GALAXIES

We study the evolution of the cold gas content of galaxies by splitting the ISM into atomic and molecular hydrogen components in the GALFORM semi-analytical model of galaxy formation (Cole et al. 2000; Benson et al. 2003; Baugh et al. 2005; Bower et al. 2006; Benson & Bower 2010; L11).

The model takes into account the main physical processes that shape the formation and evolution of galaxies. These are (i) the

collapse and merging of dark matter (DM) haloes; (ii) the shock-heating and radiative cooling of gas inside DM haloes, leading to the formation of galactic discs; (iii) quiescent SF in galaxy discs; (iv) feedback from supernovae (SNe), from active galactic nucleus (AGN) heating and from photoionization of the intergalactic medium; (v) chemical enrichment of stars and gas; and (vi) galaxy mergers driven by dynamical friction within common DM haloes which can trigger bursts of SF, leading to the formation of spheroids (for a review of these ingredients, see Baugh 2006; Benson 2010). Galaxy luminosities are computed from the predicted SF and chemical enrichment histories using a stellar population synthesis model. Dust extinction at different wavelengths is calculated self-consistently from the gas and metal contents of each galaxy and the predicted scalelengths of the disc and bulge components using a radiative transfer model (see Cole et al. 2000 and Lacey et al. 2011).

We base our study on the scheme of L11 in which parameter-free SF laws were implemented in GALFORM. In the following four subsections, we briefly describe the DM merger trees, the GALFORM models considered, the main features introduced by L11 into GALFORM and the importance of the treatment of the ISM made in this work.

2.1 DM halo merger trees

GALFORM requires the formation histories of DM haloes to model galaxy formation (see Cole et al. 2000). To generate these histories, we use an improved version of the Monte Carlo scheme of Cole et al. (2000), which was derived by Parkinson, Cole & Helly (2008). The Parkinson et al. scheme is tuned to match merger trees extracted from the Millennium Simulation of Springel et al. (2005). In this approach, realizations of the merger histories of haloes are generated over a range of halo masses. The range of masses simulated changes with redshift in order to follow a representative sample of haloes, which cover a similar range of abundances at each epoch.

By using Monte Carlo generated merger histories, we can extend the range of halo masses considered beyond the resolution limit of the Millennium Simulation, in which the smallest resolved halo mass is $\approx 10^{10}\,h^{-1}\,\mathrm{M}_{\odot}$ at all redshifts. This is necessary to make an accurate census of the global cold gas density of the universe which is dominated by low-mass galaxies in low-mass haloes (Power et al. 2010; Kim et al. 2011; L11).

We adopt a minimum halo mass of $M_{\rm halo} = 5 \times 10^8\,h^{-1}\,\mathrm{M}_{\odot}$ at $z = 0$ to enable us to predict cold gas mass structures down to the current observed limits (i.e. $M_{\rm H\,I} \approx 10^6\,\mathrm{M}_{\odot}$, Martin et al. 2010). At higher redshifts, this lower limit is scaled with redshift to roughly track the evolution of the break in the halo MF, so that we simulate objects with a comparable range of space densities at each redshift. This allows us to follow a representative sample of DM haloes, ensuring that we resolve the structures rich in cold gas at every redshift. Power et al. (2010) showed that using a fixed tree resolution, as imposed by N-body simulations, can lead to a substantial underestimate of the gas content of the universe at $z \gtrsim 3$.

The cosmological parameters are input parameters for the galaxy formation model and influence the parameter values adopted to describe the galaxy formation physics. The two models used in this paper have somewhat different cosmological parameters for historical reasons; these cannot be homogenized without revisiting the choice of the galaxy formation parameters. The parameters used in Baugh et al. (2005) are a present-day matter density of $\Omega_{\rm m} = 0.3$, a cosmological constant $\Omega_{\Lambda} = 0.7$, a baryon density of $\Omega_{\rm baryons} = 0.04$, a Hubble constant $h = 0.7$ and a power spectrum normalization of $\sigma_8 = 0.93$. In the case of Bower et al. (2006), $\Omega_{\rm m} = 0.25$, $\Omega_{\Lambda} = 0.75$, $\Omega_{\rm baryons} = 0.045$, $h = 0.73$ and $\sigma_8 = 0.9$.

2.2 Galaxy formation models

We use as starting points the Baugh et al. (2005) and Bower et al. (2006) models, hereinafter referred to as the Bau05 and Bow06 models, respectively. The most important differences between these models reside in the mechanism used to suppress SF in massive galaxies and the form of the stellar initial mass function (IMF) adopted in starbursts. The Bau05 model invokes superwinds driven by SNe, which expel gas from the halo with a mass ejection rate proportional to the SFR. The Bow06 model includes a treatment of the heating of halo gas by AGNs that suppresses gas cooling in haloes where the central black hole has an Eddington luminosity which exceeds the cooling luminosity by a specified factor. The Bau05 model assumes that the IMF is top-heavy during starbursts (driven by galaxy mergers) and has a Kennicutt (1983) form during quiescent SF in galactic discs. The Bow06 model assumes a universal Kennicutt IMF (see Almeida, Baugh & Lacey 2007; González et al. 2009; Lacey et al. 2011 for a detailed comparison between the two models). Both models give good agreement with the observed $b_{\rm J}$- and K-band LFs at $z = 0$, but only the Bow06 model agrees with the K-band LF at $z > 0.5$, regardless of the SF law used (see L11). The insensitivity of the LF of galaxies in optical and near-IR bands to the choice of the SF law was already noted by L11 and interpreted as the result of an interplay between the different channels of SF activity in the model (i.e. burst and quiescent modes).

An important modification made in this work with respect to the original assumptions of the Bau05 and Bow06 models resides in the parameters for the reionization model, following Lacey et al. (2011). It is assumed that no gas is allowed to cool in haloes with a circular velocity below $V_{\rm crit}$ at redshifts below $z_{\rm reion}$ (Benson et al. 2003). Taking into account recent simulations by Okamoto, Gao & Theuns (2008) and observational constraints on the reionization redshift (Spergel et al. 2003), we adopt $V_{\rm crit} = 30\,\mathrm{km\,s^{-1}}$ and $z_{\rm reion} = 10$, in contrast with the values adopted by Baugh et al. (2005) and Bower et al. (2006) ($V_{\rm crit} = 50$–$60\,\mathrm{km\,s^{-1}}$ and $z_{\rm reion} = 6$). Even though this affects the gas content of low-mass haloes, the changes are not significant for the results shown in this paper.

2.3 The ISM and SF in galaxies

We use the SF scheme implemented in GALFORM by L11. L11 tested different SF laws in which the neutral hydrogen in the ISM is split into H I and H_2. Two of the most promising are (i) the BR empirical SF law; and (ii) the theoretical SF law of Krumholz et al. (2009). We briefly describe these below.

(i) The empirical SF law of BR is of the form

$$\Sigma_{\rm SFR} = \nu_{\rm SF} f_{\rm mol} \Sigma_{\rm gas}, \quad (1)$$

where $\Sigma_{\rm SFR}$ and $\Sigma_{\rm gas}$ are the surface densities of the SFR and total cold gas mass, respectively, $\nu_{\rm SF}$ is the inverse of the SF time-scale for the molecular gas and $f_{\rm mol} = \Sigma_{\rm mol}/\Sigma_{\rm gas}$ is the molecular-to-total gas mass surface density ratio. The molecular and total gas contents include the contribution from helium, while H I and H_2 include only hydrogen (which in total corresponds to a fraction $X_{\rm H} = 0.74$ of the overall cold gas mass). The ratio $f_{\rm mol}$ depends on the internal hydrostatic pressure as $\Sigma_{\rm H_2}/\Sigma_{\rm H\,I} = f_{\rm mol}/(f_{\rm mol} - 1) = (P_{\rm ext}/P_0)^{\alpha}$. The values of $\nu_{\rm SF} = (5.25 \pm 2.5) \times 10^{-10}\,\mathrm{yr^{-1}}$ (Leroy et al. 2008;

Bigiel et al. 2011), $\alpha = 0.92 \pm 0.07$ and $\log(P_0/k_B\,[\mathrm{cm^{-3}\,K}]) = 4.54 \pm 0.07$ (BR), where k_B is Boltzmann's constant, are derived from fits to the observational data. To calculate P_{ext}, we use the approximation from Elmegreen (1993):

$$P_{ext} \approx \frac{\pi}{2} G \Sigma_{gas} \left[\Sigma_{gas} + \left(\frac{\sigma_g}{\sigma_\star} \right) \Sigma_\star \right], \quad (2)$$

where Σ_{gas} and $\Sigma_\star$ are the total surface densities of the gas and stars, respectively, and σ_g and $\sigma_\star$ are their respective vertical velocity dispersions. We assume a constant gas velocity dispersion, $\sigma_g = 10\,\mathrm{km\,s^{-1}}$, following recent observational results (Leroy et al. 2008). In the case of $\sigma_\star$, we assume that the self-gravity of the stellar disc is in the vertical direction, $\sigma_\star = \sqrt{\pi G h_\star \Sigma_\star}$, where $h_\star$ is the disc height (see L11 for details). We estimate $h_\star$ by assuming that it is proportional to the radial exponential scalelength of the disc, as observed in local spiral galaxies, with $R_{eff}/h_\star \approx 7.3 \pm 1.2$ (Kregel, van der Kruit & de Grijs 2002). Hereinafter, we will refer to the version of the model in which the BR empirical SF law is applied by appending BR to the model name.

(ii) In the theoretical SF law of Krumholz et al. (2009), f_{mol} in equation (1) depends on the balance between the dissociation of molecules due to the far-ultraviolet (far-UV) interstellar radiation, and their formation on the surfaces of dust grains, and ν_{SF} depends on the inverse of the time required to convert all of the gas in a cloud into stars. In their prescription, f_{mol} depends on the metallicity of the gas and the surface density of a molecular cloud, $\Sigma_{complex}$. Krumholz et al. relate $\Sigma_{complex}$ to the smooth gas surface density, Σ_{gas}, through a clumping factor that is set to $c = 5$ to reproduce the observed Σ_{SFR}–Σ_{gas} relation. In summary, the Krumholz et al. SF law is

$$\Sigma_{SFR} = \nu_{SF}(\Sigma_{gas}) f_{mol} \Sigma_{gas}, \quad (3)$$

where

$$\nu_{SF}(\Sigma_{gas}) = \nu^0_{SF} \times \left(\frac{\Sigma_{gas}}{\Sigma_0} \right)^{-0.33} \quad \text{for} \quad \Sigma_{gas} < \Sigma_0,$$
$$= \nu^0_{SF} \times \left(\frac{\Sigma_{gas}}{\Sigma_0} \right)^{0.33} \quad \text{for} \quad \Sigma_{gas} > \Sigma_0. \quad (4)$$

Here $\nu^0_{SF} = 3.8 \times 10^{-10}\,\mathrm{yr^{-1}}$ and $\Sigma_0 = 85\ \mathrm{M_\odot\,pc^{-2}}$. Hereinafter, we will denote the version of the model where the Krumholz, McKee & Tumlinson theoretical SF law is applied by KMT.

We split the total hydrogen mass component into its atomic and molecular forms and calculate the SFR based on the molecular gas mass. It is important to note that in the BR SF law, the inverse of the SF time-scale for the molecular gas, ν_{SF} (equation 1), is constant and therefore the SFR directly depends only on the molecular content and indirectly depends only on the total cold gas content through the disc pressure. However, in the KMT SF law, ν_{SF} is a function of cold gas surface density (equation 4) and therefore the SFR does depend not only on the H_2 content, but also on the cold gas surface density in a non-linear fashion.

For starbursts, the situation is less clear. Observational uncertainties, such as the conversion factor between CO and H_2 in starbursts, and the intrinsic compactness of star-forming regions, have not allowed a good characterization of the SF law (e.g. Kennicutt 1998; Genzel et al. 2010; Combes et al. 2011). Theoretically, it has been suggested that the SF law in starbursts is different from that in normal star-forming galaxies: the relation between $\Sigma_{H_2}/\Sigma_{H\,I}$ and gas pressure is expected to be dramatically different in environments of very high gas densities typical of starbursts (Pelupessy et al. 2006; Pelupessy & Papadopoulos 2009), where the ISM is predicted to be always dominated by H_2 independently of the gas pressure. For these reasons, we choose to apply the BR and KMT laws only during quiescent SF (fuelled by cooled gas accretion into galactic discs) and retain the original SF prescription for starbursts (see Cole et al. 2000 and L11 for details). In the latter, the SF time-scale is proportional to the bulge dynamical time-scale above a minimum floor value and involves the whole cold gas content of the galaxy, $\mathrm{SFR} = M_{cold}/\tau_{SF}$ (see Granato et al. 2000 and Lacey et al. 2008 for details). Throughout this work, we assume that in starbursts, the cold gas content is fully molecular, $f_{mol} = 1$. Note that this is similar to assuming that the BR pressure law holds in starbursts (except with a different ν_{SF}), given that large gas and stellar densities lead to $f_{mol} \approx 1$.

2.3.1 *Radial profiles of atomic and molecular hydrogen*

In order to visualize the behaviour of the H I and H_2 components of the ISM of galaxies predicted in the models, we have taken the output of the original Bow06 model and post-processed it to calculate the H I and H_2 surface density profiles based on the expressions above. Fig. 1 shows the surface density profiles of H I and H_2 for randomly chosen model spiral galaxies on applying the KMT (top panel) or BR (bottom panel) laws. H I extends to much larger radii than H_2. This is a consequence of the total gas surface density dependence of H_2/H I in both SF laws. Note that the KMT SF law gives a steeper decrease in the radial profile of H_2 compared to the BR SF law. The BR SF law depends on the surface density of gas and stars, through the disc pressure, while the KMT SF law depends on the surface density and metallicity of the gas.

We have compared our predictions for the size of the H I and H_2 discs with observations. The models predict a correlation between the H I isophotal radius, $l_{H\,I}$, defined at an H I surface density of $1\,\mathrm{M_\odot\,pc^{-2}}$, and the enclosed H I mass, $M_{H\,I}(l_{H\,I})$, which is in very good agreement with observations, irrespective of the SF law applied. Both models predict $M_{H\,I}(l_{H\,I})/\mathrm{M_\odot} \approx 2 \times 10^7 (l_{H\,I}/\mathrm{kpc})^{1.9}$, while the observed relation for Ursa Major is $M_{H\,I}(l_{H\,I})/\mathrm{M_\odot} \approx 1.8 \times 10^7 (l_{H\,I}/\mathrm{kpc})^{1.86}$ (e.g. Verheijen & Sancisi 2001). On the other hand, the median of the relation between the exponential scalelengths of the H_2 and H I discs predicted by the model is $R_{H_2} \approx 0.4 R_{H\,I}$, while the relation inferred by combining the

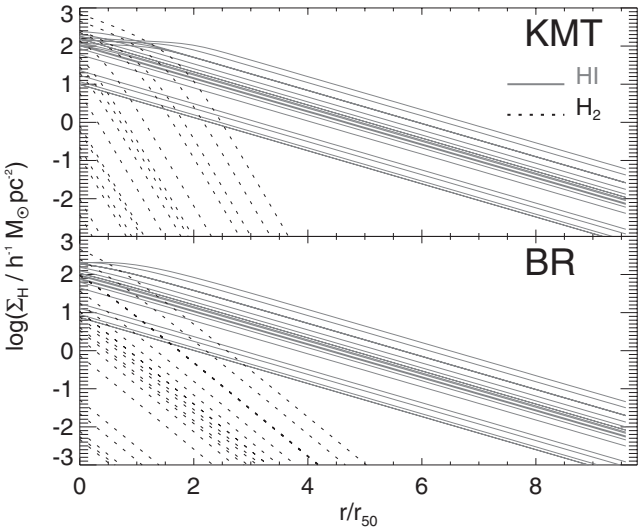

Figure 1. Surface density of H I and H_2 (solid and dashed lines, respectively) as a function of radius in units of the half-mass radius for randomly chosen galaxies in the Bow06 model, applying the KMT (top panel) and BR (bottom panel) SF laws.

observational results of Regan et al. (2001) and Verheijen & Sancisi (2001) is $R_{H_2} = (0.44 \pm 0.12) R_{H\,I}$. The model agrees well with the observed relations indicating that, in general terms, the ISM of modelled galaxies looks realistic.

2.4 Consistent calculation or post-processing?

Previous attempts to calculate the separate H I and H_2 contents of galaxies in a cosmological scenario have been made by post-processing the output of existing semi-analytic models using specifically the BR SF prescription (e.g. Obreschkow et al. 2009a; Power et al. 2010). Here we show that a self-consistent calculation of the ISM of galaxies, in which the new SF laws are included in the model, is necessary throughout in order to explain the observed gas properties of galaxies. To do this, we choose as an example the Bow06 model and the BR SF law.

Fig. 2 shows the H I MF in the original Bow06 model when a fixed conversion ratio of $M_{mol}/M_{cold} = 0.27$ is assumed (dotted line; Baugh et al. 2004), when a variable conversion factor is calculated based on the BR pressure law (dashed line), and in the Bow06.BR model (solid line), where the BR SF law is applied consistently throughout the calculation. Symbols show a compilation of observational data. The original Bow06 model with a fixed H_2/H I conversion gives a poor match to the observed H I MF. Post-processing the output of this model to implement a variable H_2/H I gives a different prediction which still disagrees with the observations. If we consistently apply the BR SF law throughout the whole galaxy formation model, there is a substantial change in the model prediction which is also in much better agreement with the observations. These differences are mainly due to the fact that the SFR in the prescription of Bow06 scales linearly with the total cold gas mass (as in starbursts, see Section 2.3), while in the case of the BR SF law, this dependence is non-linear. Note that a threshold in gas surface density below which galaxies are not allowed to form stars, as originally proposed by Kennicutt (1989) and as assumed in several other semi-analytic models (e.g. Croton et al. 2006; Tecce et al. 2010), produces a much less pronounced, but still present dip (see L11). Thus, the linearity of the SFR with cold gas mass is the main driver of the strong dip at low H I masses in the original model. Remarkably, our new modelling helps reproduce the observed number density even down to the current limits, $M_{H\,I} \approx 10^6\,h^{-2}\,M_\odot$.

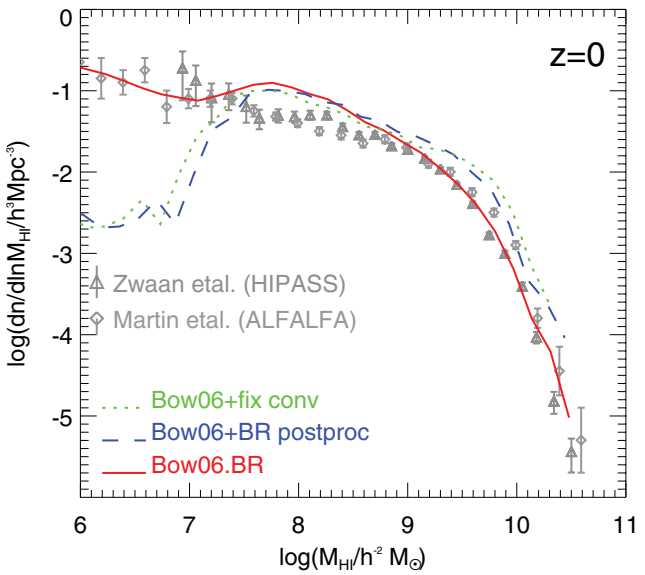

Figure 2. The H I MF at $z = 0$ for the original Bow06 model when constant $M_{mol}/M_{cold} = 0.27$ ratio is assumed (dotted line), when a variable conversion factor based on the BR pressure law is assumed (dashed line), and for the Bow06.BR model (solid line), where the BR SF law is consistently applied throughout the calculation. Symbols show observational results at $z = 0$ from Zwaan et al. (2005) using the HIPASS and Martin et al. (2010) using the ALFALFA, as labelled.

The new SF scheme to model the ISM of galaxies represents a step forward in understanding the gas content of galaxies. In the rest of this paper, we make use of the models where the parameter-free SF laws are applied throughout the full calculation.

3 SCALING RELATIONS FOR THE ATOMIC AND MOLECULAR CONTENTS OF GALAXIES IN THE LOCAL UNIVERSE

Here we present the model predictions for various scaling relations between H_2 and H I and other galaxy properties and compare with observations. In Section 3.1, we show how the H_2/H I scales with stellar and cold gas mass. In Section 3.2, we present predictions for this ratio as a function of galaxy morphology, and in Section 3.3, we study the dependence of the H I and H_2 masses on stellar mass.

3.1 The dependence of H_2/H I on galaxy mass

The prescriptions described in Section 2 that split the ISM into its atomic and molecular components enable the model to directly predict correlations between the H_2/H I and galaxy properties. Fig. 3 shows H_2/H I as a function of stellar mass (top panels) and total cold gas mass (bottom panels) at $z = 0$ for the Bow06 (solid lines) and the Bau05 (dashed lines) models using the BR and the KMT SF laws. The model predictions are compared to local observational

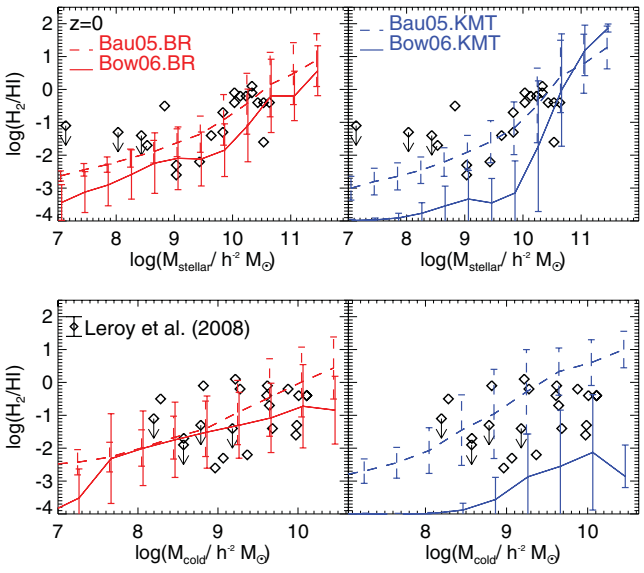

Figure 3. H_2/H I as a function of stellar mass (top panels) and total cold gas mass (M_{cold} = He + H I + H_2; bottom panels) for the two model variants, the Bow06 (solid lines) and Bau05 (dashed lines) models, when applying the BR (left-hand panels) and the KMT (right-hand panels) SF laws. The lines show the medians of the predicted distributions, while the error bars show the 10 and 90 percentiles. The grey symbols show observations of spiral and irregular galaxies from Leroy et al. (2008). The symbols with arrows represent upper limits in the observed sample. Indicative error bars in the observational sample are shown in the bottom left-hand panel.

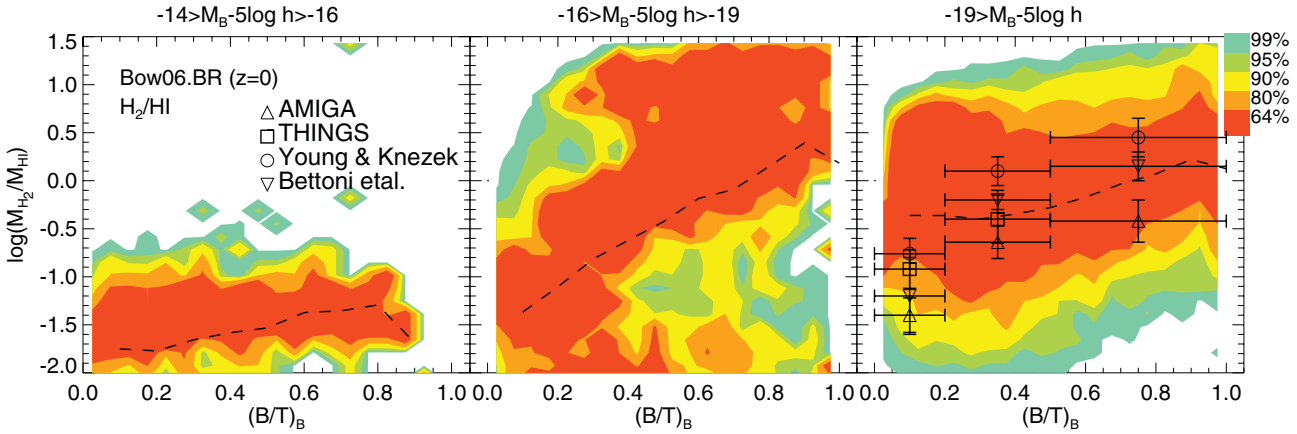

Figure 4. $M_{\rm H_2}/M_{\rm H\,I}$ as a function of B/T in the B band, $(B/T)_B$, in the Bow06.BR model, for galaxies with absolute B-band magnitudes, $M_B - 5\log(h)$, in the range indicated on top of each panel. Contours show the regions within which different volume-weighted percentages of the galaxies lie for a given $(B/T)_B$, with the scale shown by the key. For reference, the dashed line shows the median of the model distribution. Observational results from Young & Knezek (1989), Bettoni et al. (2003), Leroy et al. (2008) and Lisenfeld et al. (2011) are shown as symbols in the right-hand panel, and we combine them so that $B/T < 0.2$ corresponds to Irr, Sm and Sd galaxies; $0.2 < B/T < 0.5$ corresponds to Sc, Sb and Sa galaxies; and $B/T > 0.5$ corresponds to E and S0 galaxies (see de Vaucouleurs et al. 1991 for a description of each morphological type).

estimates from Leroy et al. (2008). The error bars in the model show the 10 and 90 percentiles of the model distribution in different mass bins. In the case of the observations, indicative error bars on the H_2/H I estimate due to the uncertainty in the CO–H_2 conversion factor are shown at the top left-hand side of the top left-hand panel (i.e. the difference between the values inferred for starbursts and the Milky Way, ≈0.6 dex; see Section 4.2). Note that in this and subsequent figures where we compare with observations, we plot masses in units of $h^{-2}\,{\rm M}_\odot$ to match observational units. For other plots, we use the simulation units, $h^{-1}\,{\rm M}_\odot$.

Leroy et al. estimated stellar masses from 3.6-μm luminosities, which were transformed into K-band luminosities using an empirical conversion. Stellar masses were then calculated from the relation of Bell et al. (2003) between the stellar mass-to-light ratio in the K band and $B - V$ colour.[1] Thus, the error on the stellar mass might be as large as a factor of 1.5 (considering the dispersion of 0.15 dex in the $B - V$ versus K-band relation).

The Bow06 model with the BR SF law predicts values of H_2/H I which are in very good agreement with the observed ones. The Bow06.KMT model fails to match the observed values of H_2/H I at all stellar and cold gas masses. This is due to the sharp decline of the radial profile of H_2 (see Fig. 1), which results in lower global values of H_2/H I in disagreement with the observed ones. In the case of the Bow06.BR model, it might appear unsurprising that this model is in good agreement with the observed correlation, given that it is based on the empirical correlation between H_2/H I and the hydrostatic pressure in the disc (see Section 2). However, it is only because we are able to reproduce other galaxy properties, such as stellar MFs (see Section 2), gas fractions and, approximately, galaxy sizes (L11), that we also predict the observed trend in the scaling relations shown in Fig. 3.

Both the Bau05.BR and Bau05.KMT models also show good agreement with the observed values of H_2/H I. The success of the Bau05.KMT model, in contrast with the Bow06.KMT model, is mainly due to the higher gas masses and metallicites predicted in the former model. However, the Bau05.BR and Bau05.KMT models fail to reproduce the evolution of the K-band LF and the $z = 0$ gas-to-luminosity ratios (see L11 for a complete discussion of the impact of each SF law on the two models).

[1] Given that Leroy et al. adopt a Kroupa (2001) IMF, we apply a small correction of 1.02 to adapt their stellar masses to account for our choice of a Kennicutt (1983) IMF.

3.2 The dependence of H_2/H I on galaxy morphology

It has been shown observationally that H_2/H I correlates strongly with the morphological type, with early-type galaxies characterized by higher values of H_2/H I than late-type galaxies (e.g. Young & Knezek 1989; Bettoni, Galletta & García-Burillo 2003; Lisenfeld et al. 2011). Fig. 4 shows H_2/H I as a function of the bulge-to-total luminosity ratio in the B band, B/T, for different B-band absolute magnitude ranges for the Bow06.BR model. The right-hand panel of Fig. 4, which shows the brightest galaxies, compares the model predictions with observations. All observational data have morphological types derived from a visual classification of the B-band images (de Vaucouleurs et al. 1991), and have also been selected in blue bands (e.g. Simien & de Vaucouleurs 1986; Weinzirl et al. 2009). The comparison with observational data is shown for galaxies in the model with $M_B - 5\log(h) < -19$, which roughly corresponds to the selection criteria applied in the observational data. Note that we have plotted only those galaxies in the model that have $M_{\rm H\,I}/M_\star \geq 10^{-3}$ and $M_{\rm H_2}/M_\star \geq 10^{-3}$, which correspond to the lowest H I and H_2 gas fractions detected in the observational data shown. The Bow06.BR model predicts a relation between H_2/H I and B/T that is in good agreement with the observations. Note that, for the last bin, $B/T < 0.2$, the model predicts slightly higher median values of H_2/H I than the values inferred from observations. However, in all cases, a constant CO (1–0)–H_2 conversion factor was assumed in the observational sample to infer the H_2 mass. This might not be a good approximation in the low-metallicity environments typical of irregular or late-type spirals, where the H_2 mass might be underestimated if a conversion factor typical of normal spiral galaxies is applied (e.g. Boselli, Lequeux & Gavazzi 2002; see Section 4.2.1 for a discussion).

The higher values of H_2/H I in early-type galaxies can be understood in the context of the dependence of H_2/H I on the gas pressure built into the BR SF law. Even though gas fractions in early-type

galaxies are in general lower than in late-type galaxies, they are also systematically more compact than a late-type counterpart of the same mass (see L11), resulting in higher gas pressure, and consequently a higher H_2/H I. Also note that there is a dependence on galaxy luminosity: faint galaxies typically have lower H_2/H I than their bright counterparts. This is due to the contribution of the stellar surface density to the pressure, which increases in massive galaxies (see equation 2).

3.3 The relation between H I, H_2 and stellar mass

Another form of scaling relation often studied observationally is the atomic or molecular hydrogen-to-stellar mass ratio as a function of stellar mass. Recently, these relations have been reported for the atomic and molecular gas contents in a homogeneous sample of relatively massive galaxies by Catinella et al. (2010) and Saintonge et al. (2011), respectively, with the aim of establishing fundamental relations between the stellar content of galaxies and their cold gas mass. Fig. 5 shows these relations for the Bow06.BR model at $z = 0$ compared to values reported for individual galaxies in these surveys with detected H_2 or H I, respectively.[2] Also shown in the top panel are a data compilation from the literature presented in Bothwell et al. (2009) and individual galaxies from the HERA CO Line Extragalactic Survey (HERACLES; Leroy et al. 2009). Measurements of $M_{H_2}/M_{stellar}$ are subject to large errors (up to 0.25 dex), given the uncertainty in the CO–H_2 conversion factor (see discussion in Section 4.2.1). Observed $M_{HI}/M_{stellar}$ are more accurate, given the direct detection of H I. The horizontal lines in Fig. 5 show representative observational sensitivity limits (which are not exactly the same in all samples). Contours show the regions where different fractions of galaxies in the model lie, normalized in bins of stellar mass. The contours are not very sensitive to the location of the sensitivity limits. The model predicts the right location and scatter of galaxies in these planes in contrast to previous models (see Saintonge et al. 2011 for a discussion). Note that the literature compilation of Bothwell et al. shows larger scatter than the HERACLES, GALEX Arecibo SDSS Survey (GASS) and CO Legacy Database for the GASS (COLD GASS). Saintonge et al. suggest that this is due to the inhomogeneity of the literature compilation.

$M_{H_2}/M_{stellar}$ in the model is only weakly correlated with stellar mass, in contrast to $M_{HI}/M_{stellar}$ which is strongly dependent on stellar mass, in agreement with the observations. The decrease in $M_{HI}/M_{stellar}$ with increasing stellar mass is the dominant factor in determining the positive relation between H_2/H I and stellar mass in Fig. 3, given the small variations of $M_{H_2}/M_{stellar}$ with stellar mass.

The predicted relation between M_{H_2} and $M_\star$ (top panel of Fig. 5) is close to linear for galaxies with $M_{H_2}/M_\star \gtrsim 0.05$. These galaxies lie on the active star-forming sequence in the $M_\star$–SFR plane (see L11), due to an approximately linear relation between M_{H_2} and SFR, although characterized by a large scatter (see Section 4.2.3). What drives the approximately constant SFR/$M_\star$ and $M_{H_2}/M_\star$ for galaxies on the active star-forming sequence is the balance between accretion and outflows, mainly regulated by the time-scale for gas to be reincorporated into the host halo after ejection by SNe (see L11 for details). In the case of H I, the model predicts that, for galaxies plotted in the bottom panel of Fig. 5, H I weakly correlates with stellar mass, $M_{HI} \propto M_\star^{0.15}$, as a result of the feedback mechanisms included in the model.

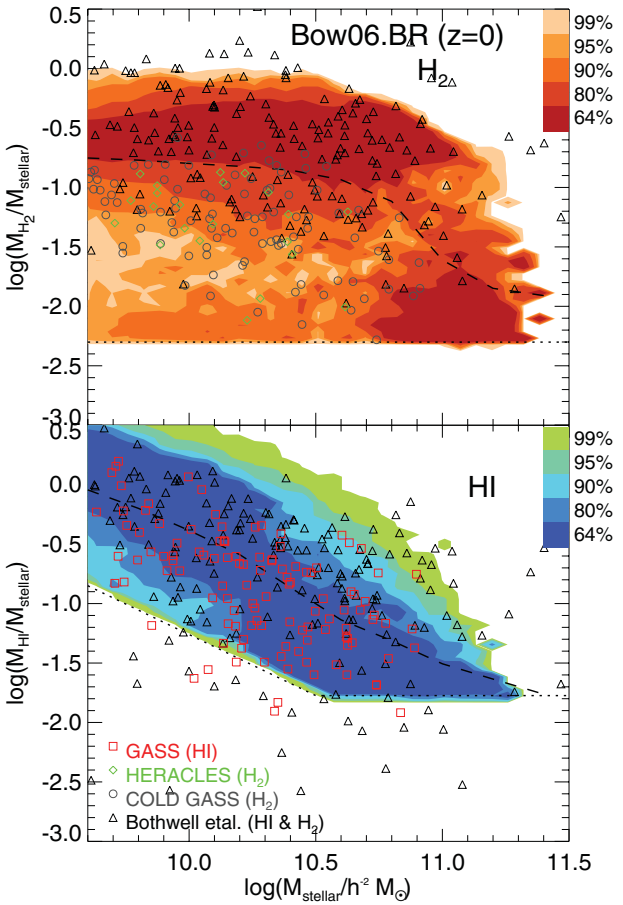

Figure 5. Top panel: molecular hydrogen-to-stellar mass ratio as a function of stellar mass for the Bow06.BR model at $z = 0$. The horizontal dotted line shows an approximate sensitivity limit below which CO (1–0) is not detected in the different molecular surveys. Contours show the regions within which different volume-weighted percentages of the galaxies lie for a given stellar mass and above the sensitivity limit, with the scale shown by the key. For reference, the dashed line shows the median of the model distributions. Observational data from the HERACLES (Leroy et al. 2009), COLD GASS (Saintonge et al. 2011) and the literature compilation of Bothwell et al. (2009) are shown as symbols. Bottom panel: as in the top panel, but for the atomic hydrogen-to-stellar mass ratio. Observational data from the GASS catalogue (Catinella et al. 2010) and the literature compilation of Bothwell et al. are shown as symbols. The dotted line shows the H I sensitivity limit of the GASS catalogue.

4 ATOMIC AND MOLECULAR HYDROGEN MASS FUNCTIONS

The two-phase ISM scheme implemented in GALFORM (see Section 2) allows us to study the evolution of H I and H_2 in galaxies in terms of the MFs and their evolution. In the next two subsections, we analyse the main mechanisms which shape the H I and H_2 MFs and investigate how these interplay to determine the model predictions.

4.1 Atomic hydrogen MF

Fig. 6 shows the $z = 0$ H I MFs for the Bow06 and Bau05 models using the BR and the KMT SF laws, and observational results from Zwaan et al. (2005) and Martin et al. (2010).

[2] Stellar masses in the observational samples were inferred using a Chabrier IMF. We scale them by a factor of 0.89 to adapt them to our choice of a Kennicutt IMF.

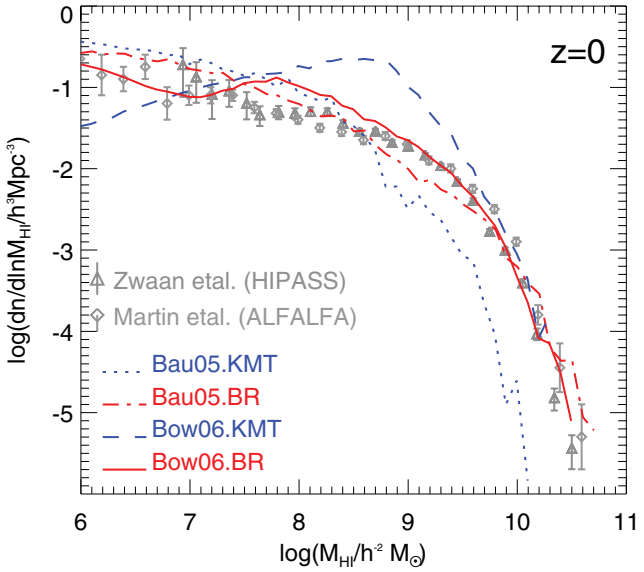

Figure 6. The H I MF at $z = 0$ for the Bau05.KMT (dotted line), Bau05.BR (dot–dashed line), Bow06.KMT (dashed line) and Bow06.BR (solid line) models. Symbols show the $z = 0$ observational estimates from Zwaan et al. (2005) using the HIPASS and from Martin et al. (2010) using the ALFALFA, as labelled.

With the BR SF law, both the Bow06 and Bau05 models give predictions which are in reasonable agreement with the observed H I MF. However, when applying the KMT SF law, both models give a poor match to the observed H I MF, with the Bau05 model underpredicting the number density of massive H I galaxies, whilst the Bow06 model greatly overpredicts the abundance of galaxies around $M_{\rm H\,I} \sim 10^9\,h^{-2}\,{\rm M}_\odot$. The latter is expected from the poor agreement between the H_2/H I–stellar mass scaling relation predicted by Bow06.KMT and the observed one (Fig. 3). In the case of Bau05.KMT, the poor agreement is expected from the low gas-to-luminosity ratios reported by L11.

Cook et al. (2010) showed that, by including the BR SF law self-consistently in their semi-analytic model, the number density of low-H I-mass galaxies is substantially increased, in agreement with our results. However, in their model, this effect is still not enough to bring the predictions into agreement with the observed H I MF. The overproduction of low-mass galaxies is also seen in their predicted optical LFs, suggesting that the difference resides in the treatment of SN feedback and reionization (see Bower et al. 2006; Benson & Bower 2010). In the case of the KMT SF law, there are no published results using the full SF law in semi-analytical models. Fu et al. (2010) implemented the H_2/H I metallicity and gas surface density dependence of the KMT SF law, but assumed a constant SF time-scale for the molecular gas, instead of the original dependence on gas surface density (see equation 4). Furthermore, these authors compared their predictions to the observations of the H I MF only over the restricted range $10^9 \lesssim M_{\rm H\,I}/h^{-2}\,{\rm M}_\odot \lesssim 10^{10}$, one decade in mass compared to the five decades plotted in Fig. 6, so that it is hard to judge how well this KMT-like model really performs.

Given that neither of the models using the KMT SF law predicts the right H I MF or H_2/H I scaling relations, and that the Bau05 model fails to predict the right K-band LF at $z > 0.5$, we now focus on the Bow06.BR model when presenting the predictions for the gas contents of galaxies at low and high redshifts.

4.1.1 *The composition of the H I MF*

The low-mass end of the $z = 0$ H I MF ($M_{\rm H\,I} \lesssim 10^7\,h^{-2}\,{\rm M}_\odot$) is dominated by satellite galaxies, as can be seen in the top panel of Fig. 7. Central galaxies contribute less to the number density in this mass range due to reionization. Hot gas in haloes with circular velocity $V_{\rm circ} < 30\,{\rm km\,s^{-1}}$ is not allowed to cool at $z < 10$, thereby suppressing the accretion of cold gas on to central galaxies hosted by these haloes. These haloes have masses typically $M_{\rm halo} < 10^{11}\,h^{-1}\,{\rm M}_\odot$ (Benson 2010). This suggests that the H I content of galaxies in isolation may lead to constraints on reionization (Kim et al., in preparation). The H I MF of satellite galaxies does not show the dip at low H I masses observed in the H I MF of central galaxies because the satellites were mainly formed before reionization. Galaxies of intermediate and high H I mass mainly correspond to central galaxies. The predominance in the H I MF of central and

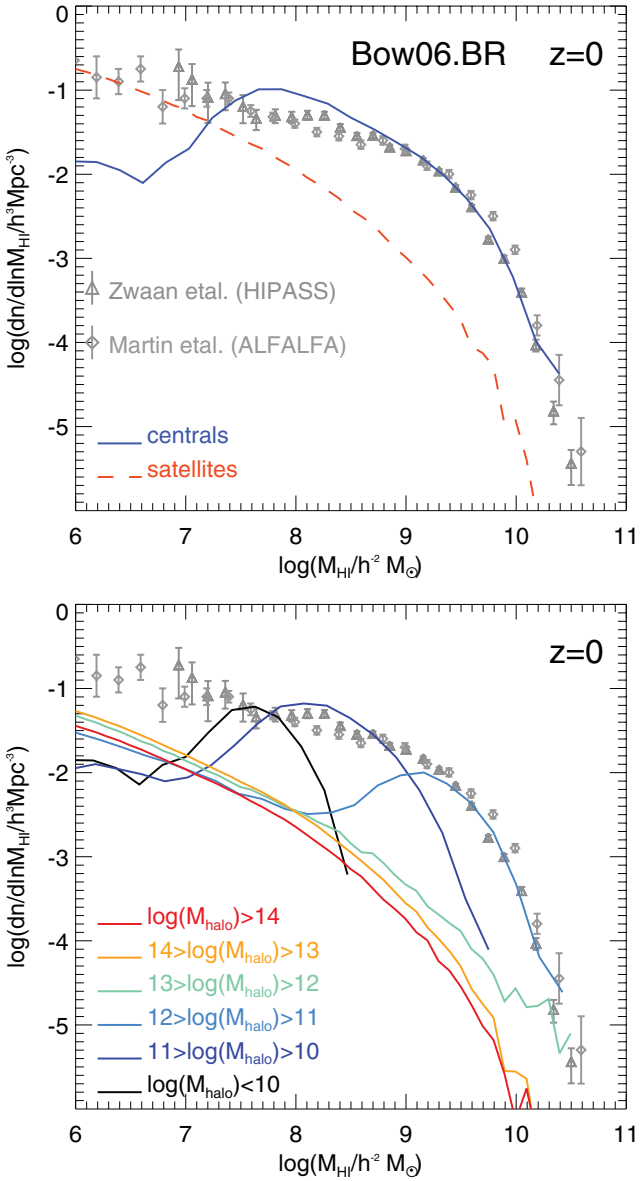

Figure 7. The H I MF at $z = 0$ in the Bow06.BR model, distinguishing between the contribution from central (solid line) and satellite (dashed line) galaxies in the top panel, and from galaxies hosted by DM haloes of different masses, as labelled, in the bottom panel.

satellite galaxies in the high- and low-mass ends, respectively, is independent of the model adopted.

The Bow06.BR model slightly overpredicts the number density of galaxies in the mass range $3 \times 10^7 < M_{\rm H\,I} < 3 \times 10^8\,h^{-2}\,{\rm M}_\odot$. This is mainly due to the slightly larger radii of the model galaxies compared to observations (see L11), which leads to lower pressure within the galactic disc and therefore to a slight overestimate of the atomic hydrogen content.

The bottom panel of Fig. 7 shows the contribution to the H I MF from galaxies hosted by haloes of different masses. The H I MF at intermediate and high H I masses, that is, $M_{\rm H\,I} \gtrsim 5 \times 10^7\,h^{-2}\,{\rm M}_\odot$, is dominated by galaxies hosted by low- and intermediate-mass DM haloes, $M_{\rm halo} \lesssim 10^{12}\,h^{-1}\,{\rm M}_\odot$, while lower H I mass galaxies are primarily satellites in higher mass haloes. This scale in the DM halo mass ($M_{\rm halo} \approx 10^{12}\,h^{-1}\,{\rm M}_\odot$) has been shown to be set by the efficient suppression of SF in higher mass DM haloes, mainly driven by AGN feedback which shuts down gas cooling (Kim et al. 2011). In lower mass haloes, in which AGN feedback does not suppress gas cooling, the cold gas content scales with the stellar mass of the galaxy and with the mass of the host DM halo.

4.1.2 *Evolution of the H I MF*

Fig. 8 shows the evolution of the H I MF from $z = 8$ to 0. There is a high abundance of low-H I-mass galaxies at high redshift. This reduces with declining redshift as gas is depleted mainly through quiescent SF and starbursts. The number density of galaxies with low H I masses, $M_{\rm H\,I} \lesssim 10^7\,h^{-2}\,{\rm M}_\odot$, increases with redshift, being a factor of 4 larger at $z = 6$ than at $z = 0$. The number density of H I galaxies with masses $10^7 \lesssim M_{\rm H\,I} \lesssim 10^8\,h^{-2}\,{\rm M}_\odot$ increases by a factor of 2 from $z = 0$ to 1, with little evolution to $z = 4$. At $z > 4$, the number density of galaxies in this mass range drops again. The high-mass end of the H I MF, $M_{\rm H\,I} \gtrsim 5 \times 10^8\,h^{-2}\,{\rm M}_\odot$, grows hierarchically until $z \approx 1$, increasing in number density by more than two orders of magnitude. The evolution of the high-mass end tracks the formation of more massive haloes in which gas can cool, until AGN heating becomes important (at $z \approx 1$). At $z < 1$, the high-mass end does not show appreciable evolution. The H I MF from the break upwards in mass is dominated by galaxies in intermediate-mass haloes. These are less affected by AGN feedback, driving the hierarchical growth in the number density in the high H I mass range. Higher mass haloes, $M_{\rm halo} \gtrsim 10^{12}\,h^{-1}\,{\rm M}_\odot$, are subject to AGN feedback, which suppresses the cooling flow and reduces the cold gas reservoir in the central galaxies of these haloes. Lower mass haloes, $M_{\rm halo} \lesssim 10^{11}\,h^{-1}\,{\rm M}_\odot$, are susceptible to SN feedback, which depletes the cold gas supply by heating the gas and returning it to the hot halo.

Note that our choice of parameters for reionization affects mainly the low-mass end of the MF at high redshifts. At $z = 0$, the abundance of galaxies with $M_{\rm H\,I} \lesssim 10^8\,h^{-2}\,{\rm M}_\odot$ would be lower by a factor of 2 if a lower photoionization redshift cut of $z_{\rm reion} = 6$ were assumed.

The characterization of the H I MF at redshifts higher than $z \approx 0$ will be a difficult task in future observations. The first measurements will come from the stacking of stellar-mass- or SFR-selected galaxy samples, as has been done in the local Universe (e.g. Lah et al. 2007, 2009; Verheijen et al. 2007). Fig. 9 shows the cumulative H I mass per unit volume, $\rho_{\rm H\,I}$, at different redshifts for samples of galaxies in the Bow06.BR model that have stellar masses or SFRs larger than $M_{\rm stellar}$ or SFR, respectively. The estimated $\rho_{\rm H\,I}$ from source stacking can be directly compared to our predictions for the same lower stellar mass or SFR limit. The median H I mass of galaxies as a function of stellar mass and SFR is shown in the bottom panels of Fig. 9. The

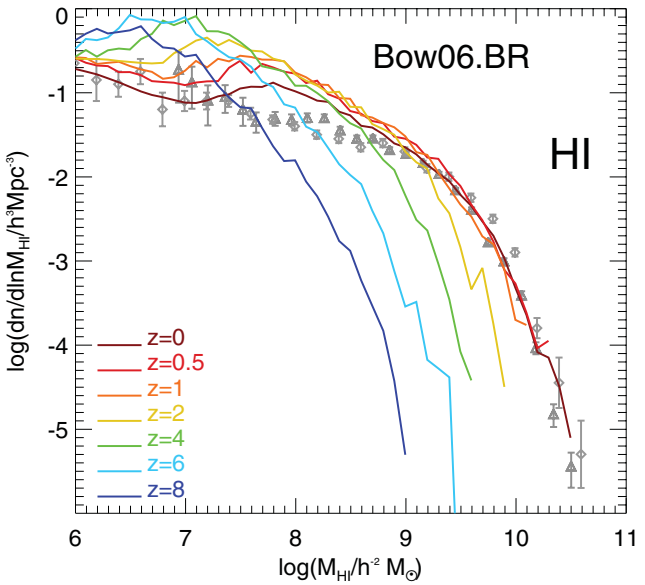

Figure 8. The H I MFs for the Bow06.BR model at different redshifts, as labelled. For reference, we show the $z = 0$ observational results from Zwaan et al. (2005) and Martin et al. (2010).

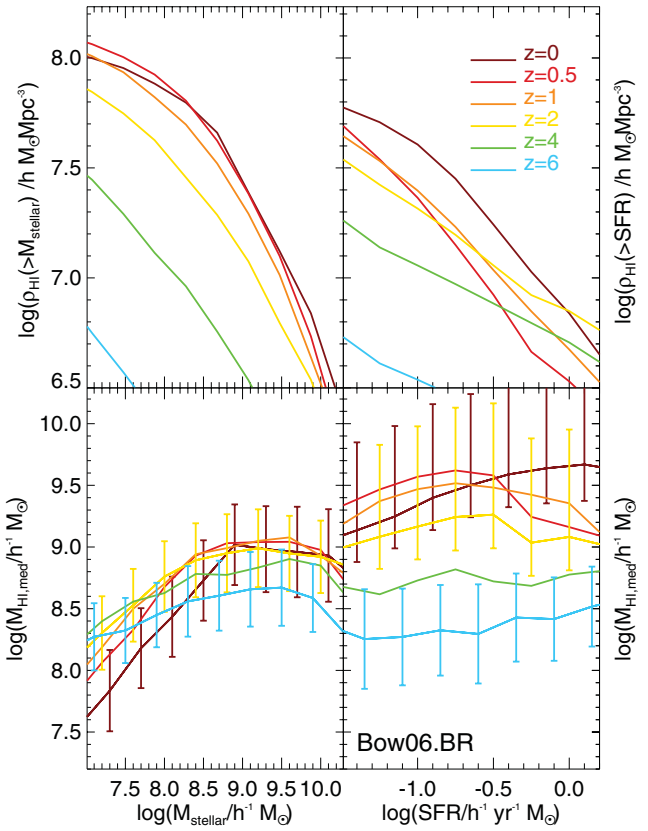

Figure 9. Top panels: cumulative H I mass density for galaxies in the Bow06.BR model with stellar masses (left-hand panel) or SFRs (right-hand panel) larger than a given value at different redshifts, as labelled. Bottom panels: median H I mass of galaxies as a function of stellar mass (left-hand panel) and SFR (right-hand panel). The error bars correspond to the 10 and 90 percentiles of the distributions, and are shown for three different redshifts.

error bars represent the 10 and 90 percentiles of the distributions, and are shown for three different redshifts. The H I mass–stellar mass relation becomes shallower with increasing redshift, but the scatter around the median depends only weakly on redshift. The turnover of the median H I mass at $M_{\rm stellar} \gtrsim 10^9\,h^{-2}\,{\rm M}_\odot$ is produced by AGN feedback that efficiently suppresses any further gas cooling on to massive galaxies and, consequently, their cold gas content is reduced. The H I mass is weakly correlated with SFR, particularly at high redshift. The median H I mass of galaxies spanning SFRs in the range plotted decreases with increasing redshift. This suggests that in order to detect low H I masses in observations at $z \approx 0.5$–2, stellar-mass-selected samples should be more effective than SFR-selected samples. However, it would still be necessary to sample down to very low stellar masses ($M_{\rm stellar} > 10^8\,h^{-1}\,{\rm M}_\odot$). Upcoming H I surveys using telescopes such as the ASKAP and MeerKAT will be able to probe down to these H I masses.

4.2 Molecular hydrogen MF

The cold gas content is affected not only by SF, feedback processes and accretion of new cooled gas, but also by the evolution of galaxy sizes, given that our prescriptions to calculate the H_2 abundance depend explicitly on the gas density (see Section 2.3). Our aim is to disentangle which processes primarily determine the evolution of H_2 in galaxies.

4.2.1 The present-day CO (1–0) LF

Observationally, the most commonly used tracer of the H_2 molecule is CO, and, in particular, the CO (1–0) transition which is emitted in the densest, coldest regions of the ISM, where H_2 is locked up. Given that in the model we estimate the H_2 content, we use a conversion factor to estimate the CO (1–0) emission for a given abundance of H_2:

$$I_{\rm CO}/{\rm K\,km\,s^{-1}} = \frac{N_{\rm H_2}/{\rm cm^{-2}}}{X \times 10^{-20}}. \quad (5)$$

Here $N_{\rm H_2}$ is the column density of H_2 and $I_{\rm CO}$ is the integrated CO (1–0) line intensity per unit surface area. The value of X has been inferred observationally in a few galaxies, mainly through virial estimations. Typical estimates for normal spiral galaxies range between $X \approx 2.0$–3.5 (e.g. Young & Scoville 1991; Boselli et al. 2002; Blitz et al. 2007). However, systematic variations in the value of X are both theoretically predicted and observationally inferred. For instance, theoretical calculations predict that low metallicities, characteristic of dwarf galaxies, or high densities and large optical depths of molecular clumps in starburst galaxies, should change X by a factor of up to 5–10 in either direction (e.g. Bell, Viti & Williams 2007; Meijerink, Spaans & Israel 2007; Bayet et al. 2009). Observations of dwarf galaxies favour larger conversion factors (e.g. $X \approx 7$; e.g. Boselli et al. 2002), while the opposite holds for starburst galaxies (e.g. $X \approx 0.5$; e.g. Meier & Turner 2004). This suggests a metallicity-dependent conversion factor X. However, estimates of the correlation between X and metallicity in nearby galaxies vary significantly, from finding no correlation, when virial equilibrium of giant molecular clouds (GMCs) is assumed (e.g. Young & Scoville 1991; Blitz et al. 2007), to correlations as strong as $X \propto ({\rm Z/Z_\odot})^{-1}$, when the total gas content is inferred from the dust content on assuming metallicity-dependent dust-to-gas ratios (e.g. Guelin et al. 1993; Boselli et al. 2002).

We estimate the CO (1–0) LF by using different conversion factors favoured by the observational estimates described above. The top panel of Fig. 10 shows the CO (1–0) LF at $z = 0$ when different constant conversion factors are assumed (i.e. independent of galaxy properties; solid lines). Observational estimates of the CO (1–0) LF, made using a B-band and a 60-μm-selected sample, are plotted using symbols (Keres et al. 2003). The model slightly underestimates the number density at $L^\star$ for $X > 1$, but gives good agreement at fainter and brighter luminosities for sufficiently large values of X (such as the ones inferred in normal spiral galaxies). In the predicted CO (1–0) LF, we include all galaxies with $L_{\rm CO} > 10^3$ Jy km s^{-1} Mpc^2, while the LFs from Keres et al. were inferred from samples of galaxies selected using 60-μm or B-band fluxes. These criteria might bias the LF towards galaxies with large amounts of dust or large recent

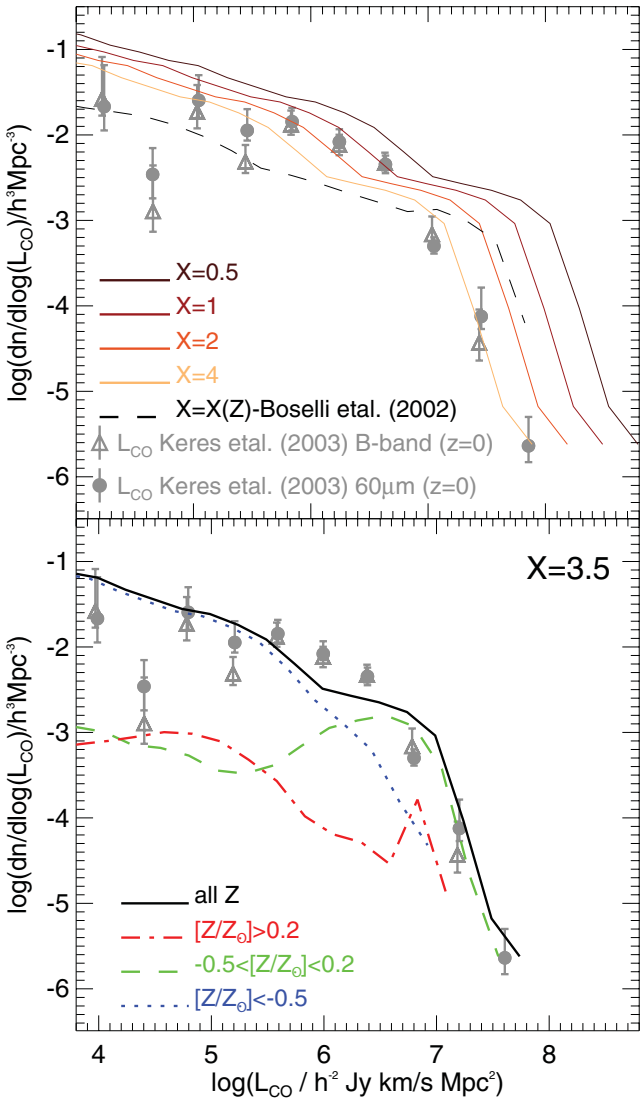

Figure 10. The CO (1–0) LF at $z = 0$ for the Bow06.BR model compared to the observational estimates of Keres et al. (2003) for B-band-selected (triangles) and 60-μm-selected (filled circles) samples of galaxies. To calculate the CO (1–0) luminosities, we assume a H_2-to-CO conversion factor, X, where $N_{\rm H_2}/{\rm cm^{-2}} = X \times 10^{-20} I_{\rm CO}/{\rm K\,km\,s^{-1}}$. In the top panel, the solid lines show the model predictions using fixed values of X, as labelled, and the dashed line shows the LF using the metallicity-dependent conversion factor, $X(Z)$, of Boselli et al. (2002). In the bottom panel, the solid line shows the LF resulting from a conversion factor $X = 3.5$ and the different lines show the contribution of galaxies in different metallicity ranges, as labelled, for this choice of X.

SF. More data are needed from blind CO surveys in order to characterize the CO LF in non-biased samples of galaxies. This will be possible with new instruments such as the LMT.

In order to illustrate how much our predictions for the CO (1–0) LF at $z = 0$ vary when adopting a metallicity-dependent conversion factor, $X(Z)$, inferred independently from observations, we also plot in the top panel of Fig. 10 the LF when the $X(Z)$ relation from Boselli et al. (2002) is adopted (dashed line), $\log(X) = 0.5^{+0.2}_{-0.2} - 1.02^{+0.05}_{-0.05}\log(Z/Z_\odot)$. Note that this correlation was determined using a sample of 12 galaxies with CO (1–0) luminosities in quite a narrow range, $L_{CO} \approx 5 \times 10^5$–$5 \times 10^6$ Jy km s^{-1} Mpc^2. On adopting this conversion factor, the model largely underestimates the break of the LF. This is due to the contribution of galaxies with different metallicities to the CO (1–0) LF, as shown in the bottom panel of Fig. 10. The faint end is dominated by low-metallicity galaxies ($Z < Z_\odot/3$), while high-metallicity galaxies ($Z > Z_\odot/3$) dominate the bright end. A smaller X for low-metallicity galaxies combined with a larger X for high-metallicity galaxies would give better agreement with the observed data. However, such a dependence of X on metallicity is opposite to that inferred by Boselli et al.

By considering a dependence of X on metallicity alone, we are ignoring possible variations with other physical properties which could influence the state of GMCs, such as the interstellar far-UV radiation field and variations in the column density of gas (see, for instance, Pelupessy et al. 2006; Bayet et al. 2009; Pelupessy & Papadopoulos 2009; Papadopoulos 2010). Recently, Obreschkow et al. (2009b) showed that by using a simple phenomenological model to calculate the luminosity of different CO transitions, which includes information about the ISM of galaxies, the CO (1–0) LF of Fig. 10 can be reproduced. However, this modelling introduces several extra free parameters into the model which, in most cases, are not well constrained by observations. A more detailed calculation of the CO LF which takes into account the characteristics of the local ISM environment is beyond the scope of this paper and is addressed in a forthcoming paper (Lagos et al., in preparation).

For simplicity, in the next subsection, we use a fixed CO (1–0)–H_2 conversion factor of $X = 3.5$ for galaxies undergoing quiescent SF and $X = 0.5$ for those experiencing starbursts. In the case of galaxies undergoing both SF modes, we use $X = 3.5$ and 0.5 for the quiescent and the burst components, respectively, following the discussion above.

4.2.2 *Evolution of the H_2 MF*

At high redshift, measurements of the CO ($J \rightarrow J - 1$) LF are not currently available. The ALMA will, however, provide measurements of molecular emission lines in high-redshift galaxies with high accuracy. We therefore present in Fig. 11 predictions for the H_2 MF and CO (1–0) LF up to $z = 8$.

The high-mass end of the H_2 MF shows strong evolution from $z = 8$ to 4, with the number density of galaxies increasing by an order of magnitude. In contrast, the number density of low-H_2-mass galaxies stays approximately constant over the same redshift range. From $z = 4$ to 2, the H_2 MF hardly evolves, with the number density of galaxies remaining the same over the whole mass range. From $z = 2$ to 0, the number density of massive galaxies decreases by an order of magnitude, while the low-mass end decreases only by a factor of ≈3. The peak in the number density of massive H_2 galaxies at $z = 2$–3 coincides with the peak of the SF activity (see Fanidakis et al. 2010; L11), in which huge amounts of H_2 are consumed forming new stars. The following decrease in the number density at $z < 2$ overlaps with strong galactic-size evolution, where galaxies at lower redshift are systematically larger than their high-redshift counterparts, reducing the gas surface density and hence the H_2 fraction. We return to this point in Section 5. The peak in the number density of high-H_2-mass galaxies at $z = 2$–3 and the following decrease contrasts with the monotonic increase in the number density of high-H I-mass galaxies with time, suggesting a strong evolution of the global H_2/H I with redshift. We will come back to this point in Section 6.

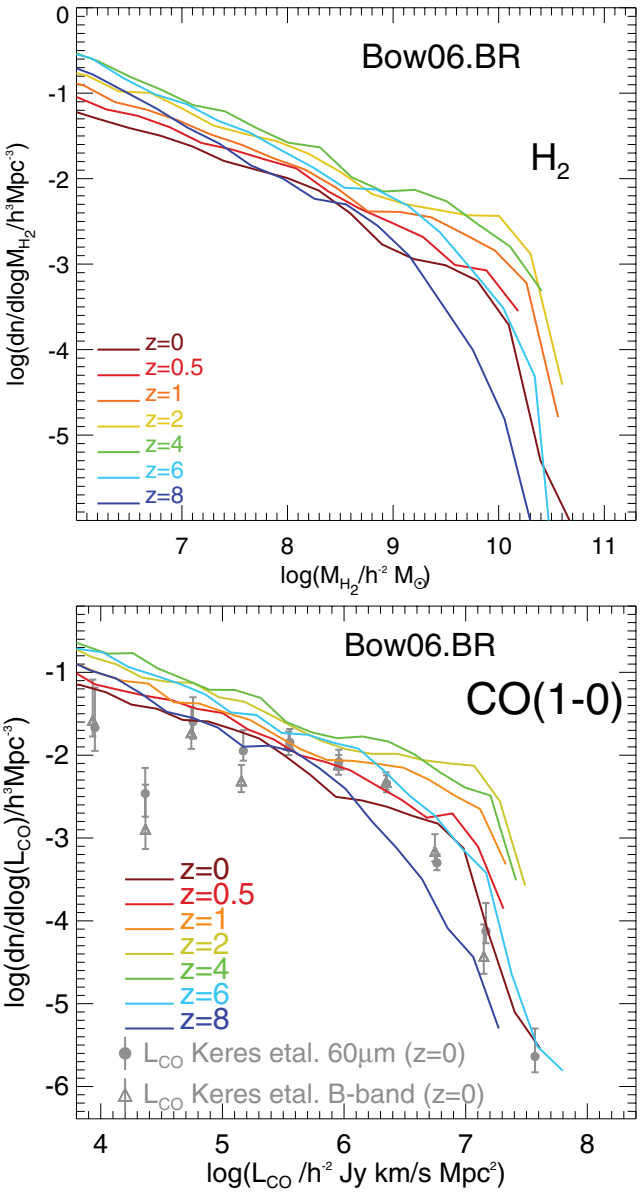

Figure 11. The H_2 MF (top panel) and the CO (1–0) LF (bottom panel) at different redshifts, as labelled, for the Bow06.BR model. Two fixed CO (1–0)–H_2 conversion factors are assumed: $X = 3.5$ for quiescent SF and $X = 0.5$ for burst SF. For reference, we show the CO (1–0) LFs estimated at $z = 0$ by Keres et al. (2003) from *B*-band-selected and 60-μm-selected galaxy samples.

The evolution of the CO (1–0) LF with redshift is shown in the bottom panel of Fig. 11. Note that the $z = 0$ LF is very similar to the one shown in the bottom panel of Fig. 10, in which we assume a fixed CO–H_2 conversion $X = 3.5$ for all galaxies. This is due to the low number of starburst events at $z = 0$. However, at higher

redshifts, starbursts contribute more to the LF; the most luminous events at high redshift, in terms of CO luminosity, correspond to starbursts (see Section 4.2.3).

Recently, Geach et al. (2011) compared the evolution of the observed molecular-to-(stellar plus molecular mass) ratio (which approximates to the gas-to-baryonic ratio if the H I fraction is small), $f_{\rm gas} = M_{\rm mol}/(M_{\rm stellar} + M_{\rm mol})$, with predictions for the Bow06.BR model at $z \leq 2$, and found that the model gives a good match to the observed $f_{\rm gas}$ evolution after applying the same observational selection cuts.

4.2.3 *The IR–CO luminosity relation*

One way to study the global relation between the SFR and the molecular gas mass in galaxies, and hence to constrain the SF law, is through the relation between the total IR luminosity, $L_{\rm IR}$, and the CO (1–0) luminosity, $L_{\rm CO}$. We here define the total IR luminosity to be an integral over the rest-frame wavelength range 8–1000 μm, which approximates the total luminosity emitted by interstellar dust, free from contamination by starlight. In dusty star-forming galaxies, most of the UV radiation from young stars is absorbed by dust, and this dominates the heating of the dust, with only a small contribution to the heating from older stars. Under these conditions, and if there is no significant heating of the dust by an AGN, we expect that $L_{\rm IR}$ should be approximately proportional to the SFR, with a proportionality factor that depends mainly on the IMF. On the other hand, as already discussed, the CO (1–0) luminosity has been found observationally to trace the molecular gas mass in local galaxies, albeit with a proportionality factor that is different in starbursts from quiescently star-forming galaxies. Observations suggest that submillimetre galaxies (SMGs) and QSOs at high redshift lie on a similar IR–CO luminosity relation to luminous IR galaxies (LIRGs) and ultraluminous IR galaxies (ULIRGs) observed in the local Universe (see Solomon & Vanden Bout 2005 for a review). We investigate here whether our model predictions are consistent with these observational results.

We show in Fig. 12 the predicted IR–CO (1–0) luminosity relation, $L_{\rm IR}$–$L'_{\rm CO}$, for the Bow06.BR model at different redshifts, compared to observational data for different types of galaxies. The predicted CO (1–0) luminosities for the model galaxies are calculated from their H_2 masses as given in Section 4.2.1, using conversion factors $X = 3.5$ for quiescent galaxies and $X = 0.5$ for starbursts. To facilitate the comparison with observations, we here express the CO luminosities $L'_{\rm CO}$ in units of K km s^{-1} pc^2, which corresponds to expressing the CO line intensity as a brightness temperature. We predict the IR luminosities of the model galaxies using the method described in Lacey et al. (2011) and González et al. (2011) (see also Lacey, Baugh & Frenk, in preparation), which uses a physical model for the dust extinction at each wavelength to calculate the total amount of stellar radiation absorbed by dust in each galaxy, which is then equal to its total IR luminosity. The dust model assumes a two-phase ISM, with star-forming clouds embedded in a diffuse medium. The total mass of dust is predicted by GALFORM self-consistently from the cold gas mass and metallicity, assuming a dust-to-gas ratio which is proportional to the gas metallicity, while the radius of the diffuse dust component is assumed equal to that of the star-forming component, whether a quiescent disc or a burst, and is also predicted by GALFORM.

We show the model predictions in Fig. 12 separately for quiescent (left-hand panel) and starburst galaxies (right-hand panel), where quiescent galaxies are defined as those whose the total SFR

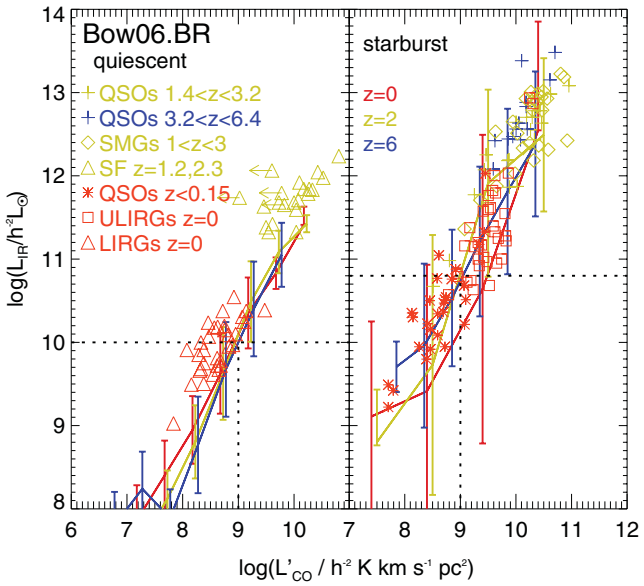

Figure 12. Infrared luminosity as a function of the CO (1–0) luminosity for the Bow06.BR model at $z = 0$ (red lines), $z = 2$ (yellow lines) and $z = 6$ (blue lines) for quiescent (left-hand panel) and starburst galaxies (right-hand panel). The solid lines show the median, while the error bars show the 10 and 90 percentiles of the distributions. To aid the comparison between the quiescent and starburst galaxies, the dotted lines show the predicted median IR luminosity at $z = 2$ for a CO luminosity of $10^9\ h^{-2}$ K km s^{-1} pc^2. We also show the following observational data: local LIRGs from Gao & Solomon (2004) (triangles); local ULIRGs from Solomon et al. (1997) (squares); QSOs at $z \lesssim 0.15$ from Scoville et al. (2003), Evans et al. (2006) and Bertram et al. (2007) (asterisks); star-forming galaxies at $z \approx 1.2$ and $z \approx 2.3$ from Tacconi et al. (2010) and Genzel et al. (2010) (triangles); SMGs at $1 \lesssim z \lesssim 3$ from Greve et al. (2005), Solomon & Vanden Bout (2005) and Tacconi et al. (2006) (diamonds); and QSOs at $1.4 \lesssim z \lesssim 6.4$ from Riechers (2011) (crosses). Note that most of the observational data on the CO(1–0) luminosity at high redshifts are inferred from the luminosities of higher CO transitions rather than being directly measured.

is dominated by SF taking place in the galactic disc (i.e. $\mathrm{SFR_{disc}} > \mathrm{SFR_{burst}}$). The solid lines show the median of the predicted IR–CO relation at different redshifts, while the error bars represent the 10 and 90 percentiles of the distributions. To facilitate the comparison between quiescent and starburst galaxies, the typical IR luminosity at a CO luminosity of $10^9\ h^{-2}$ K km s^{-1} pc^2 is shown as the dotted lines in both panels. We see that the separate $L_{\rm IR}$–$L'_{\rm CO}$ relations for quiescent and starburst galaxies depend only slightly on redshift, but that the relation for starbursts is offset to higher IR luminosities than for quiescent galaxies. There are two contributions to this offset in the model. The first is the different SF laws assumed in starbursts and in galaxy discs. By itself, this results in roughly 40 times larger IR luminosities at a given H_2 mass for starbursts. However, as already described, we also assume a CO-to-H_2 conversion factor X which is seven times smaller in starbursts, which causes an offset in the $L_{\rm IR}$–$L'_{\rm CO}$ relation in the opposite sense. The combination of these two effects results in a net offset of roughly a factor of 6 in $L_{\rm IR}$ at a given $L'_{\rm CO}$.

A similar bimodality in the IR–CO luminosity plane has also been inferred observationally by Genzel et al. (2010) and Combes et al. (2011). However, these results rely on inferring the CO (1–0) luminosities from higher CO transitions when the lowest transitions

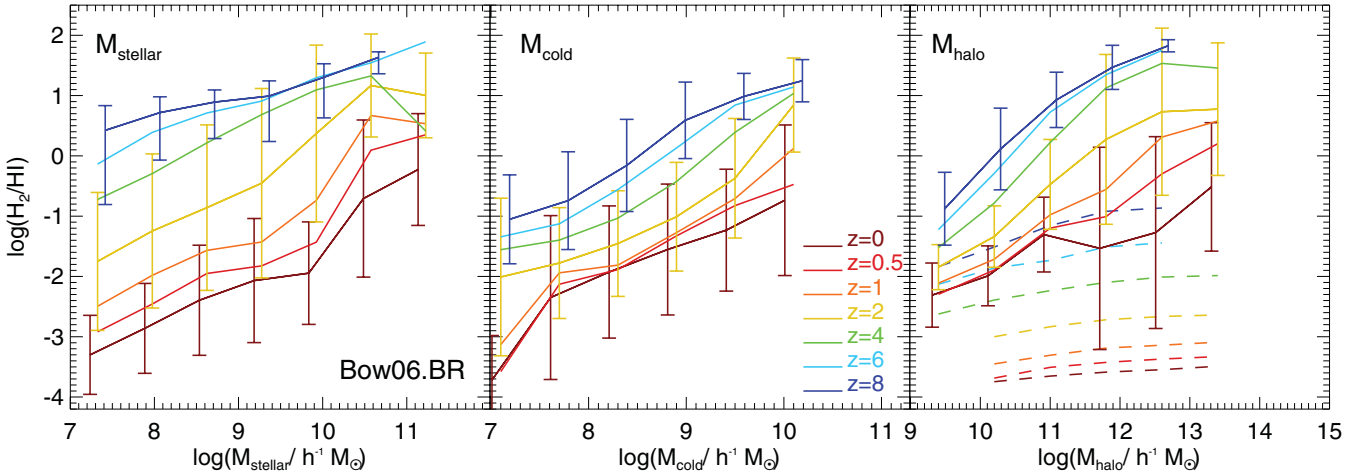

Figure 13. H_2/H I as a function of stellar mass (left-hand panel), cold gas mass (middle panel) and DM halo mass (right-hand panel) at different redshifts, as labelled, for the Bow06.BR model. The lines show the medians of the distributions, while the error bars show the 10–90 percentile ranges. For clarity, these error bars are plotted only for three different redshifts. In the right-hand panel, central and satellite galaxies are shown separately as the solid and dashed lines, respectively. The error bars are shown only for central galaxies in this panel.

are not available, which could be significantly uncertain, as we discuss below (see also Ivison et al. 2011).

For comparison, we also plot in Fig. 12 a selection of observational data. We plot data for local LIRGs and UV/optically selected star-forming galaxies at $z \sim 1$–2 in the left-hand panel to compare with the model predictions for quiescent galaxies, and for local ULIRGs and SMGs at $z \sim 1$–3, and QSOs at $z \sim 0$–6 in the right-hand panel to compare with the model predictions for starbursts. We note that there are important uncertainties in the observational data plotted for high-redshift ($z > 1$) objects. For these, the IR luminosities are actually inferred from observations at a single wavelength (24 or 850 μm), using an assumed shape for the spectral energy distribution of dust emission. [In addition, the Riechers (2011) data on $z > 1$ QSOs are actually for far-IR, that is, 40–120 μm, luminosities, rather than total IR luminosities.] Furthermore, the CO (1–0) luminosities for $z > 1$ objects are in most cases also not direct measurements, but are instead inferred from measurements of higher CO transitions $J \rightarrow J - 1$ (usually $4 \rightarrow 3$ or $3 \rightarrow 2$). The conversion from $L'_{\rm CO}$ ($J \rightarrow J - 1$) to $L'_{\rm CO}$ (1–0) is usually done assuming that the brightness temperature of the CO line is independent of the transition $J \rightarrow J - 1$, as would be the case if the CO lines are emitted from an optically-thick medium in thermal equilibrium at a single temperature (as appears to be the case in local spiral galaxies). In this case, the luminosity $L'_{\rm CO}$ is independent of the transition studied (Solomon & Vanden Bout 2005). However, recent observations have shown different brightness temperatures for different CO transitions in some high-redshift galaxies (Danielson et al. 2010; Ivison et al. 2011). As a result, there could be large errors in the CO (1–0) luminosities of high-redshift galaxies when they are inferred from higher transitions.

Comparing the model predictions for the IR–CO relation with the observational data, we see that the predictions for quiescent galaxies at $z = 0$ are in broad agreement with the observations of nearby LIRGs, while at $z = 2$, the model predicts partially the location of UV/optically selected star-forming galaxies. In the case of starburst galaxies, the predicted relation agrees with the observations of low-redshift ULIRGs and high-redshift SMGs, and also with the observations of QSOs at both low and high redshift. The latter is consistent with the suggestion from observations that QSOs follow the same $L_{\rm IR}$–$L'_{\rm CO}$ relation as starburst galaxies (e.g. Evans et al. 2006; Riechers 2011). The model is thus able to explain the $L_{\rm IR}$–$L'_{\rm CO}$ relation for all objects without needing to include any heating of dust by AGNs. This also agrees with previous theoretical predictions which concluded that only higher CO transitions are affected by the presence of an AGN (e.g. Meijerink et al. 2007; Obreschkow et al. 2009b).

5 EVOLUTION OF SCALING RELATIONS OF H_2/H I

Our model predicts that the H I and H_2 MFs are characterized by radically different evolution with redshift. This implies strong evolution of H_2/H I. In this section, we analyse scaling relations of H_2/H I with galaxy properties and track the evolution of these relations towards high redshift with the aim of understanding what drives them.

Fig. 13 shows the median H_2/H I as a function of stellar mass, cold gas mass and halo mass at different redshifts for the Bow06.BR model. The error bars indicate the 10 and 90 percentiles of the model distribution in different mass bins. In the right-hand panel, the predictions for satellite and central galaxies are shown separately as the dashed and solid lines, respectively. For clarity, percentile ranges are shown only for central galaxies in this panel. In the case of satellites, the spread around the median is usually larger than it is for central galaxies.

Fig. 13 shows that H_2/H I correlates strongly with stellar and cold gas mass in an approximately power-law fashion. The normalization of the correlation between H_2/H I and stellar mass (left-hand panel of Fig. 13) evolves by two to three orders of magnitude from $z = 8$ to 0 towards smaller values. The evolution is milder (only ≈1.5 dex) if one focuses instead on the correlation with cold gas mass. Interestingly, the slope of the correlation between H_2/H I and stellar or cold gas mass hardly evolves. The approximate scalings of H_2/H I against stellar and cold gas mass are

$$\mathrm{H_2/H\,I} \approx 0.01 \left(\frac{M_{\rm stellar}}{10^{10}\, h^{-1}\, \mathrm{M_\odot}} \right)^{0.8} (1+z)^{3.3}, \quad (6)$$

$$\mathrm{H_2/H\,I} \approx 0.09 \left(\frac{M_{\rm cold}}{10^{10}\, h^{-1}\, \mathrm{M_\odot}} \right)^{0.9} (1+z)^{2.4}. \quad (7)$$

Note that the relation with $M_{\rm stellar}$ is only valid up to $z = 4$. At higher redshifts, the slope of the correlation becomes shallower. The relation with $M_{\rm cold}$, however, has the same slope up to $z = 8$. The normalization of the relation of H_2/H I with $M_{\rm stellar}$ has a stronger dependence on redshift compared to the relation with $M_{\rm cold}$. However, note that the distribution around the median is quite broad, as can be seen from the percentile range plotted in Fig. 13, so these expressions have been taken just as an illustration of the evolution of the model predictions.

The trend between H_2/H I of galaxies and host halo mass depends strongly on whether central or satellite galaxies are considered. In the case of central galaxies (solid lines in the right-hand panel of Fig. 13), there is a correlation between H_2/H I and halo mass that becomes shallower with decreasing redshift in intermediate- and high-mass haloes ($M_{\rm halo} > 5 \times 10^{11}\, h^{-1}\, {\rm M}_\odot$). This change in slope is mainly due to the fact that at lower redshift ($z \lesssim 1.5$), AGN feedback strongly suppresses SF in central galaxies hosted by haloes in this mass range, so that the stellar mass–halo mass correlation also becomes shallower and with an increasing scatter. At high redshift, the stellar mass–halo mass correlation is tighter and steeper. In the case of satellite galaxies, H_2/H I does not vary with host halo mass, but exhibits a characteristic value that depends on redshift. The lower the redshift, the lower the characteristic H_2/H I for satellites. None the less, the spread around the median, in the case of satellite galaxies, is very large, that is, of 1.5 dex at $z = 0$. The lack of correlation between H_2/H I and halo mass and the large scatter are due to the dependence of H_2/H I on galaxy properties (such as stellar and cold gas mass) rather than on the host halo mass.

In order to disentangle what causes the strong evolution of H_2/H I with redshift, we study the evolution of the galaxy properties that are directly involved in the calculation of H_2/H I. These are the disc size, cold gas mass and stellar mass, which together determines the hydrostatic pressure of the disc. Fig. 14 shows H_2/H I, the half-mass radius (r_{50}), the cold gas mass, the stellar mass and the mid-plane hydrostatic pressure of the disc at r_{50}, as functions of the cold baryonic mass of the galaxy, $M_{\rm bar} = M_{\rm stellar} + M_{\rm cold}$. These predictions are for the Bow06.BR model. Note that we only plot late-type galaxies (selected as those with $B/T < 0.5$) as these dominate the cold gas density at any redshift.

In general, galaxies display strong evolution in size, moving towards larger radii at lower redshifts. However, this evolution takes place independently of galaxy morphology, implying that the galactic-size evolution is caused by the size evolution of the host DM haloes (i.e. driven by mergers with other DM haloes and accretion of DM on to haloes). Note that the evolution in radius is about an order of magnitude from $z = 6$ to 0, which easily explains the evolution by two orders of magnitude in H_2/H I (which is $\propto P_{\rm ext}^{0.92} \propto r^{-1.84}$). By increasing the disc size, the gas density and pressure decrease and therefore the molecular fraction decreases. The evolution in cold gas mass is mild enough so as not to significantly affect H_2/H I. Observationally, galaxies of the same rest-frame UV luminosity seem to be a factor of ≈2–3 smaller at $z \approx 6$ than at $z \approx 2$ (e.g. Bouwens et al. 2004; Oesch et al. 2010), in good agreement with the factor of ≈2–3 evolution in size predicted by the Bow06.BR model (see Lacey et al. 2011, for a detailed comparison of sizes predicted by the model with the observed galaxy population).

Fig. 14 shows that the stellar mass of galaxies, at a given baryonic mass, increases with decreasing redshift and therefore the corresponding cold gas mass decreases. This drives the hydrostatic pressure to be reduced even further. The mid-plane hydrostatic pressure evaluated at r_{50}, $P_{\rm ext}(r_{50})/k_{\rm B}$ (bottom panel of Fig. 14), evolves by more than two orders of magnitude at a given $M_{\rm bar}$ over the redshift range plotted. Note that the typical values of $P_{\rm ext}(r_{50})/k_{\rm B}$ predicted at $z = 0$ are comparable to those reported in observations of nearby galaxies, $P_{\rm ext}/k_{\rm B} = 10^3$–$10^7$ cm^{-3} K (e.g. BR; Leroy et al. 2008).

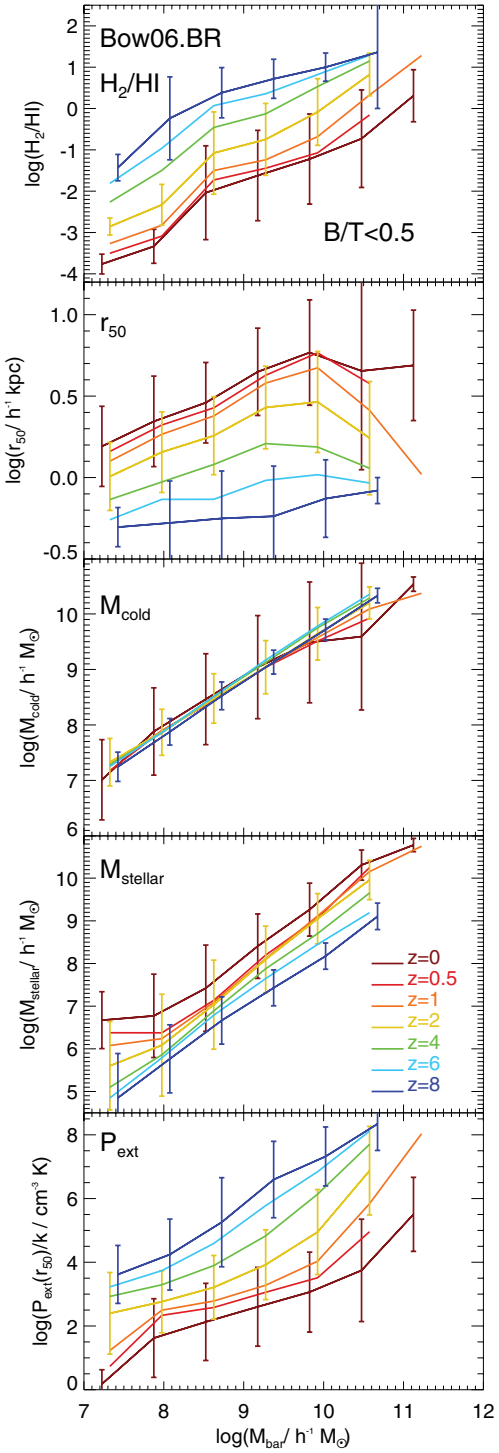

Figure 14. H_2/H I (top panel), half-mass radius, r_{50} (second panel), cold gas mass (third panel), stellar mass (fourth panel) and mid-plane hydrostatic pressure at r_{50} (bottom panel), as functions of the total cold baryonic mass in the galaxy (i.e. $M_{\rm bar} = M_{\rm stellar} + M_{\rm cold}$) at different redshifts (as labelled) for the Bow06.BR model. The solid lines show the medians of the distributions, while the error bars show the 10 and 90 percentiles, and for clarity are plotted only for three different redshifts.

At higher redshifts, the values of $P_{\rm ext}(r_{50})$ also overlap with the range in which the $\Sigma_{\rm H_2}/\Sigma_{\rm H\,I}$–$P_{\rm ext}$ correlation has been constrained observationally at $z = 0$.

The evolution in galactic size is therefore the main factor responsible for the predicted evolution in H_2/H I at a fixed baryonic mass in the model, with a minor contribution from other properties which also contribute to determining this quantity (i.e. cold gas and stellar mass).

6 COSMIC EVOLUTION OF THE ATOMIC AND MOLECULAR GAS DENSITIES

H_2/H I depends strongly on galaxy properties and redshift. In this section, we present predictions for the evolution of the global density of H I and H_2.

The top panel of Fig. 15 shows the evolution of the global comoving mean density of all forms of hydrogen (solid line), H I (dashed line) and H_2 (dot–dashed line), in units of the critical density at $z = 0$, $\rho/\rho_{c,z=0}$. Observational estimates of the H I and H_2 mass density at different redshifts and using different techniques are shown using symbols (see references in Section 1). If the reported values of $\rho_{\rm H\,I}$ and $\rho_{\rm H_2}$ include the contribution from helium, then we subtract this when plotting the data.

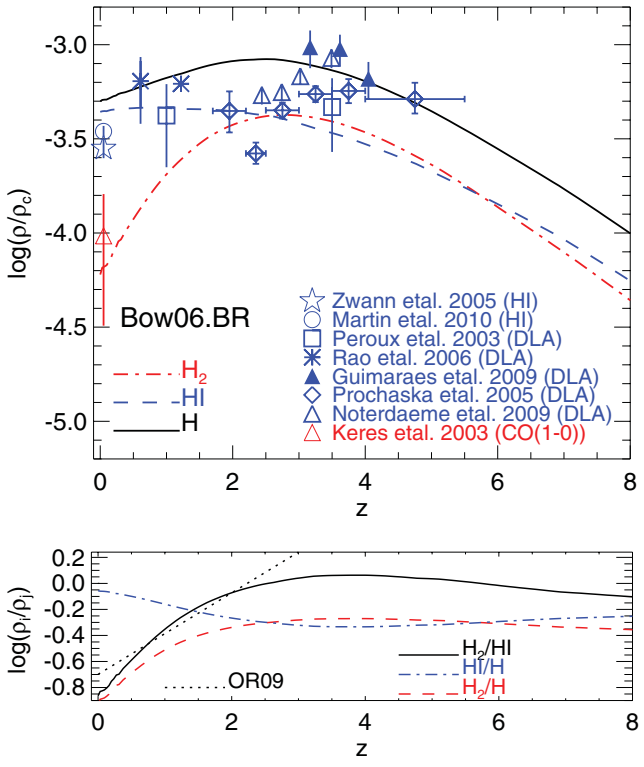

Figure 15. Top panel: global density of all forms of neutral hydrogen gas (solid line), atomic hydrogen (dashed line) and molecular hydrogen (dot–dashed line) in units of the critical density at $z = 0$, as a function of redshift for the Bow06.BR model. Observational estimates of the H I mass density plotted are from Zwaan et al. (2005) and Martin et al. (2010) from the H I MF, and Péroux et al. (2003), Prochaska et al. (2005), Rao et al. (2006), Guimarães et al. (2009) and Noterdaeme et al. (2009) from DLAs. Also shown is the local Universe estimate of the H_2 mass density from Keres et al. (2003) using the CO (1–0) LF. Bottom panel: global atomic-to-total neutral hydrogen (dot–dashed line), molecular-to-total neutral hydrogen (dashed line) and molecular-to-atomic hydrogen (solid line) mass ratios, as functions of redshift. For comparison, the evolution of the global H_2/H I predicted by Obreschkow & Rawlings (2009) is shown as a dotted line.

The top panel of Fig. 15 shows the evolution of the global comoving mean density of all forms of hydrogen (solid line), H I (dashed line) and H_2 (dot–dashed line), in units of the critical density at $z = 0$, $\rho/\rho_{c,z=0}$. Observational estimates of the H I and H_2 mass density at different redshifts and using different techniques are shown using symbols (see references in Section 1). If the reported values of $\rho_{\rm H\,I}$ and $\rho_{\rm H_2}$ include the contribution from helium, then we subtract this when plotting the data.

The model predicts local universe gas densities in good agreement with the observed ones, which is expected from the good agreement with the H I MF and CO (1–0) LF. At high redshift, the model predicts $\rho_{\rm H\,I}$ in good agreement with the observed density of H I inferred from damped Lyα systems (DLAs). Note that in our model, by definition, H I is attached to galaxies (see Section 2). However, recent simulations by Faucher-Giguère & Kereš (2011), Altay et al. (2010) and Fumagalli et al. (2011) suggest that DLAs might not correspond exclusively to the H I gas attached to galaxies, but also to H I clumps formed during the rapid accretion of cold gas (e.g. Binney 1977; Haehnelt, Steinmetz & Rauch 1998). Thus, the comparison between our predictions of $\rho_{\rm H\,I}$ and the values inferred from observations from DLAs has to be considered with caution in mind.

At $z = 0$, the H I mass density is much larger than that of H_2, due to the low molecular fractions in extended, low-pressure galactic discs. At $z \approx 2$, where galactic discs are characterized by larger pressure and therefore higher molecular fractions, the density of H_2 slightly exceeds that of H I. This H_2 domination extends up to $z \approx 5$, above which H I again becomes the principal form of neutral hydrogen. These transitions are clearly seen in the bottom panel of Fig. 15, where the evolution of the global H I/H, H_2/H and H_2/H I is shown. Note that the peak of the global H_2/H I is at $z \approx 3.5$. The predicted evolution of the global H_2/H I differs greatly from the theoretical predictions reported previously by Obreschkow & Rawlings (2009, dotted line in the bottom panel of Fig. 15) and Power et al. (2010), which were obtained from post-processed semi-analytic models (see Section 2.4). These authors reported a monotonic increase in H_2/H I with redshift, even up to global values of H_2/H I $\approx$10. This difference with our results is due in part to resolution effects, since these papers used DM haloes extracted from the Millennium Simulation (see Section 2.1) and therefore only sample haloes with $M_{\rm halo} \geq 10^{10}\,h^{-1}\,{\rm M}_\odot$ at all redshifts. Consequently, these calculations were not able to resolve the galaxies that dominate the H I global density at high redshift, inferring an artificially high global H_2/H I. We can confirm this assertion if we fix the halo mass resolution in the Bow06.BR model at $M_{\rm halo} = 10^{10}\,h^{-1}\,{\rm M}_\odot$, whereupon a global value of H_2/H I $\approx$7 is attained at $z = 8$. This is in better agreement with the value predicted by Obreschkow & Rawlings (2009), but is still $\sim$1.5 times lower. We interpret this difference as being due to the post-processing applied by Obreschkow et al. rather than the self-consistent calculation adopted here. We have already showed that post-processing can lead to answers which differ substantially from the self-consistent approach (see Fig 2). We can summarize the predicted evolution of the global H_2/H I, $\rho_{\rm H_2}/\rho_{\rm H\,I}$, as being characterized by three stages,

$$\begin{aligned}\rho_{\rm H_2}/\rho_{\rm H\,I} &\approx 0.13(1+z)^{1.7} \quad \text{for} \quad z \lesssim 2\,,\\ &\approx 0.45(1+z)^{0.6} \quad \text{for} \quad 2 \lesssim z \lesssim 4\,,\\ &\approx 3.7(1+z)^{-0.7} \quad \text{for} \quad z \gtrsim 4.\end{aligned} \tag{8}$$

Fig. 16 shows the contribution to $\rho_{\rm H\,I}$ (top panel) and $\rho_{\rm H_2}$ (bottom panel) from haloes of different mass. The overall evolution of $\rho_{\rm H\,I}$ is always dominated by low- and intermediate-mass haloes with $M_{\rm halo} < 10^{12}\,h^{-1}\,{\rm M}_\odot$. At $z > 1$, the contribution from haloes with masses of $10^{11} < M_{\rm halo} < 10^{12}\,h^{-1}\,{\rm M}_\odot$ quickly drops, and at $z > 4$, the same happens with haloes in the mass range $10^{10} < M_{\rm halo} < 10^{11}\,h^{-1}\,{\rm M}_\odot$. At higher redshifts, low-mass haloes become the primary hosts of H I mass. In contrast, the evolution of $\rho_{\rm H_2}$ is always dominated by intermediate- and high-mass haloes with

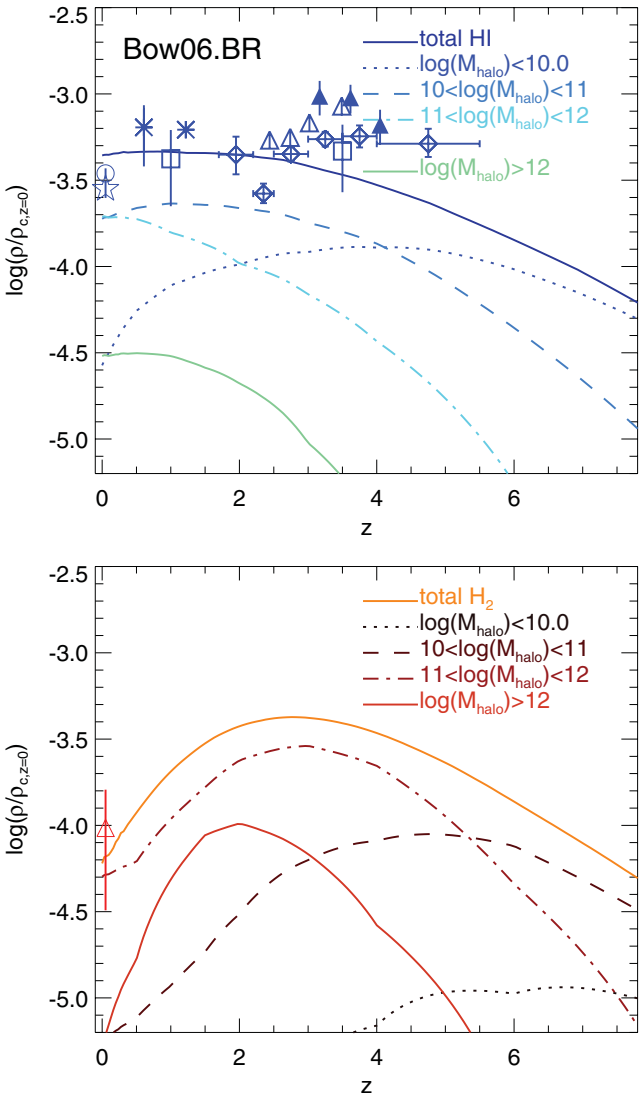

Figure 16. Global density of atomic hydrogen (top panel) and molecular hydrogen (bottom panel) in units of the critical density at $z = 0$, as a function of redshift for the Bow06.BR model. The contributions from different DM halo mass ranges are shown by different lines as labelled. Observational estimates of the total H I and H_2 mass densities are also shown. Symbols correspond to different observations as labelled in Fig. 15.

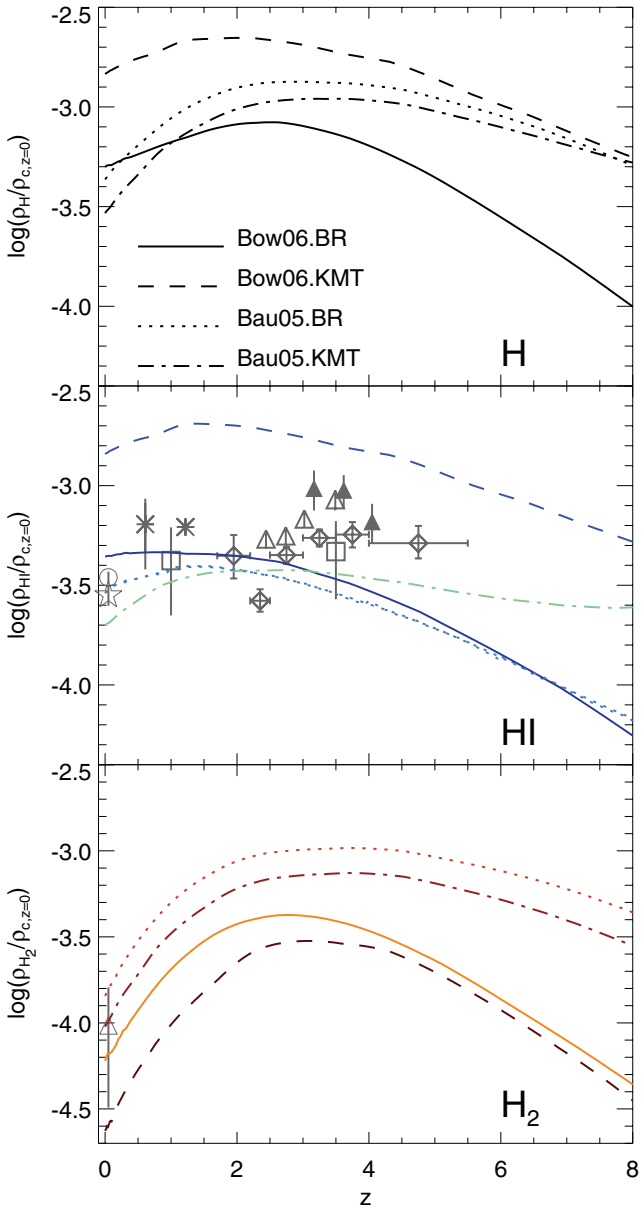

Figure 17. Global density of all forms of neutral H (top panel), H I (middle panel) and H_2 (bottom panel) in units of the critical density at $z = 0$, as a function of redshift for the Bow06.BR, Bow06.KMT, Bau05.BR and Bau05.KMT models, as labelled in the top panel. Symbols show observational estimates, as labelled in Fig. 15.

$M_{\rm DM} > 10^{11}\,h^{-1}\,{\rm M}_{\odot}$, supporting our interpretation of the evolution of the H I and H_2 MFs. This suggests that the weak clustering of H I galaxies reported by Meyer et al. (2007) and Basilakos et al. (2007) is mainly due to the fact that H I-selected galaxies are preferentially found in low-mass haloes, while in more massive haloes, the hydrogen content of galaxies has a larger contribution from H_2.

Note that the evolution of $\rho_{\rm H\,I}$ and $\rho_{\rm H_2}$ with redshift is weaker than the evolution of the SFR density, $\rho_{\rm SFR}$. As L11 reported, $\rho_{\rm SFR}$ increases by a factor of $\approx$15 from $z = 0$ to 3 (the predicted peak of the SF activity). On the other hand, $\rho_{\rm H_2}$ evolves by a factor of $\approx$7 from $z = 0$ to 3 (where the H_2 density peaks), while $\rho_{\rm H\,I}$ evolves weakly, decreasing by a factor of only 1.5 from $z = 0$ to 5. The difference in redshift evolution between $\rho_{\rm H_2}$ and $\rho_{\rm SFR}$ is due to the contribution from starbursts to the latter at $z > 2$, which drops quickly at lower redshifts. This leads to a larger decrease in the global $\rho_{\rm SFR}$ compared to $\rho_{\rm H_2}$. We remind the reader that we assume different SF laws for starbursts and quiescent SF, and therefore, by construction, different gas depletion time-scales (see Section 2.3).

In order to gain an impression of how much the predicted global density evolution can change with the modelling of SF, Fig. 17 shows the global density evolution of the neutral H, H I and H_2 for the Bau05.BR, Bau05.KMT, Bow06.BR and Bow06.KMT models. The former three models predict very similar global density evolution of H I at $z < 4$, while at higher redshifts, the Bau05.KMT model predicts larger global densities mainly due to the metallicity dependence of H_2/H I in the KMT SF law (see equation 4) and the typically lower gas metallicities in high-redshift galaxies. However, the Bow06.KMT model predicts a global density of H I offset by a factor of 4 with respect to the observational estimates and the other models over the whole redshift range. This is caused by the

large overprediction of the number density of intermediate-H I-mass galaxies by this model (Fig. 6). In the case of the global density of H_2, all the models predict a similar redshift peak at $z \approx 3$–4, but with an offset in the maximum density attained.

7 SUMMARY AND CONCLUSIONS

We have presented predictions for the H I and H_2 content of galaxies and their evolution with redshift in the context of galaxy formation in the ΛCDM framework. We use the extension of the GALFORM semi-analytic model implemented by Lagos et al. (2011) in which the neutral hydrogen in the ISM of galaxies is split into its atomic and molecular components. To do that, we have used either the empirical correlation of BR, between H_2/H I and the hydrostatic pressure of the disc, or the formalism of Krumholz et al. (2009) of molecule formation on dust grains balanced by UV dissociation. We assume that the SFR depends directly on the H_2 content of galaxies, as suggested by observational results for nearby galaxies (e.g. Wong & Blitz 2002; Solomon & Vanden Bout 2005; Bigiel et al. 2008; Schruba et al. 2010). We do not change any other model parameter, so as to isolate the consequences of changing the SF law on the model predictions.

We study the evolution of H I and H_2 predicted by two models, Bau05 and Bow06, after applying the BR or KMT SF law prescriptions. When applying the BR SF law, we find that the Bau05 and Bow06 models predict a present-day H I MF in broad agreement with observations by Zwaan et al. (2005) and Martin et al. (2010), and a relation between H_2/H I and stellar and cold gas mass in broad agreement with Leroy et al. (2008). When applying the KMT SF law, the two models fail to predict the observed H I MF at $z = 0$. Moreover, L11 find that the Bau05 model fails to predict the observed K-band LF at $z > 0.5$, regardless of the SF law assumed. Hence, we select as our best model with the BR SF law applied (Bow06.BR). This model predicts local Universe estimates of the H I and H_2 MFs, scaling relations of H_2/H I, $M_{H_2}/M_{stellar}$ and $M_{H\,I}/M_{stellar}$ with galaxy properties, and also the IR–CO luminosity relation in reasonable agreement with observations, but also gives good agreement with stellar masses, optical LFs, gas-to-luminosity ratios, among others (see L11 for a full description of the predictions of the GALFORM model when changing the SF law, and Fanidakis et al. 2010 for predictions of this model for the AGN population). We show that the new SF law applied is a key model component to reproduce the local H I MF at intermediate and low H I masses, given that it reduces SF and therefore SNe feedback, allowing the survival of larger gas reservoirs.

Using the Bow06.BR model, we can predict the evolution of the H I and H_2 MFs. We find that the evolution of H I is characterized by a monotonic increase in the number density of massive galaxies with decreasing redshift. For H_2, the number density of massive galaxies increases from $z = 8$ to 4, followed by very mild evolution down to $z = 2$. At $z < 2$, the number density in this range drops quickly. These radical differences in the H I and H_2 MF evolution are due to the strong evolution in H_2/H I with redshift, due to the dependence on galaxy properties. We also present predictions for the H I mass–stellar mass and H I mass–SFR relations, and for the cumulative H I mass density of stacked samples of galaxies selected by stellar mass or SFR at different redshifts, which is relevant to the first observations of H I expected at high redshift.

At a given redshift, H_2/H I strongly depends on the stellar and cold gas masses. The normalization of the correlation evolves strongly with redshift, increasing by two orders of magnitude from $z = 0$ up to $z = 8$, in contrast with the very mild evolution in the slope of the correlations. We also find that H_2/H I correlates with halo mass only for central galaxies, where the slope and normalization of the correlation depends on redshift. For satellite galaxies, no correlation with the host halo mass is found, which is a result of the weak correlation between satellite galaxy properties and their host halo mass. We find that the main mechanism driving the evolution of the amplitude of the correlation between H_2/H I and stellar and cold gas mass, and with halo mass in the case of central galaxies, is the size evolution of galactic discs. Lower redshift galaxies are roughly an order of magnitude larger than $z = 8$ galaxies with the same baryonic mass (cold gas and stellar mass).

Finally, we studied the cosmic density evolution of H I and H_2, and find that the former is characterized by very mild evolution with redshift, in agreement with observations of DLAs (e.g. Péroux et al. 2003; Noterdaeme et al. 2009), while the density of H_2 increases by a factor of 7 from $z \approx 0$ to $z \approx 3$. We also predict that H_2 slightly dominates over the H I content of the universe between $z \approx 2$–4 (with a peak of $\rho_{H_2}/\rho_{H\,I} \approx 1.2$ at $z \approx 3.5$), and that it is preferentially found in intermediate-mass DM haloes. On the other hand, we find that H I is mainly contained in low-mass haloes. The global H_2/H I ratio evolution with redshift is characterized by a rapid increase from $z = 0$ to 2 as $\rho_{H_2}/\rho_{H\,I} \propto (1+z)^{1.7}$, followed by a slow increase at $2 < z < 4$ as $\rho_{H_2}/\rho_{H\,I} \propto (1+z)^{0.6}$, to finally decrease slowly with increasing redshift at $z > 4$ as $\rho_{H_2}/\rho_{H\,I} \propto (1+z)^{-0.7}$. We conclude that previous studies (Obreschkow & Rawlings 2009; Power et al. 2010) overestimated this evolution due in part to halo mass resolution effects, as the galaxies which dominate the H I density at $z \gtrsim 2$ were not resolved in these calculations.

The results of this paper suggest radically different evolution of the cosmic densities of H I and H_2, as well as a strong evolution of H_2/H I in galaxies. The next generation of radio and submillimetre telescopes (such as the ASKAP, MeerKAT, SKA, LMT and ALMA) will reveal the neutral gas content of the Universe and galaxies up to very high redshifts, and will be able to test the predictions made here.

ACKNOWLEDGMENTS

We thank Richard Bower, Ian Smail, Houjun Mo, Nicolas Tejos, Gabriel Altay, Estelle Bayet and Padeli Papadopoulos for useful comments and discussions, and Rachael Livermore and Matthew Bothwell for providing the observational data of the IR–CO relation and the H I and H_2 scaling relations, respectively. We thank the anonymous referee for helpful suggestions that improved this work. CdPL gratefully acknowledges a STFC Gemini studentship. AJB acknowledges the support of the Gordon & Betty Moore Foundation. This work was supported by a rolling grant from the STFC. Part of the calculations for this paper were performed on the ICC Cosmology Machine, which is part of the DiRAC Facility jointly funded by the STFC, Large Facilities Capital Fund of BIS and Durham University.

REFERENCES

Almeida C., Baugh C. M., Lacey C. G., 2007, MNRAS, 376, 1711
Altay G., Theuns T., Schaye J., Crighton N. H. M., Dalla Vecchia C., 2010, ApJ, 737, 37
Basilakos S., Plionis M., Kovač K., Voglis N., 2007, MNRAS, 378, 301
Baugh C. M., 2006, Rep. Prog. Phys., 69, 3101
Baugh C. M., Lacey C. G., Frenk C. S., Benson A. J., Cole S., Granato G. L., Silva L., Bressan A., 2004, New Astron. Rev., 48, 1239

Baugh C. M., Lacey C. G., Frenk C. S., Granato G. L., Silva L., Bressan A., Benson A. J., Cole S., 2005, MNRAS, 356, 1191
Bayet E., Viti S., Williams D. A., Rawlings J. M. C., Bell T., 2009, ApJ, 696, 1466
Bell E. F., McIntosh D. H., Katz N., Weinberg M. D., 2003, ApJS, 149, 289
Bell T. A., Viti S., Williams D. A., 2007, MNRAS, 378, 983
Benson A. J., 2010, Phys. Rep., 495, 33
Benson A. J., Bower R., 2010, MNRAS, 405, 1573
Benson A. J., Bower R. G., Frenk C. S., Lacey C. G., Baugh C. M., Cole S., 2003, ApJ, 599, 38
Bertram T., Eckart A., Fischer S., Zuther J., Straubmeier C., Wisotzki L., Krips M., 2007, A&A, 470, 571
Bettoni D., Galletta G., García-Burillo S., 2003, A&A, 405, 5
Bigiel F., Leroy A., Walter F., Brinks E., de Blok W. J. G., Madore B., Thornley M. D., 2008, AJ, 136, 2846
Bigiel F. et al., 2011, ApJ, 730, L13
Binney J., 1977, ApJ, 215, 483
Blitz L., Rosolowsky E., 2006, ApJ, 650, 933 (BR)
Blitz L., Fukui Y., Kawamura A., Leroy A., Mizuno N., Rosolowsky E., 2007, in Reipurth B., Jewitt D., Keil K., eds, Protostars and Planets V. Univ. Arizona Press, Tucson, AZ, p. 81
Booth R. S., de Blok W. J. G., Jonas J. L., Fanaroff B., 2009, preprint (arXiv:0910.2935)
Boselli A., Lequeux J., Gavazzi G., 2002, A&A, 384, 33
Bothwell M. S., Kennicutt R. C., Lee J. C., 2009, MNRAS, 400, 154
Bouwens R. J., Illingworth G. D., Blakeslee J. P., Broadhurst T. J., Franx M., 2004, ApJ, 611, L1
Bower R. G., Benson A. J., Malbon R., Helly J. C., Frenk C. S., Baugh C. M., Cole S., Lacey C. G., 2006, MNRAS, 370, 645
Catinella B. et al., 2010, MNRAS, 403, 683
Cattaneo A., Dekel A., Faber S. M., Guiderdoni B., 2008, MNRAS, 389, 567
Chang T., Pen U., Bandura K., Peterson J. B., 2010, Nat, 466, 463
Cole S., Lacey C. G., Baugh C. M., Frenk C. S., 2000, MNRAS, 319, 168
Combes F., García-Burillo S., Braine J., Schinnerer E., Walter F., Colina L., 2011, A&A, 528, 124
Cook M., Evoli C., Barausse E., Granato G. L., Lapi A., 2010, MNRAS, 402, 941
Croton D. J. et al., 2006, MNRAS, 365, 11
Daddi E. et al., 2010, ApJ, 713, 686
Danielson A. L. R. et al., 2010, MNRAS, 410, 1687
de Vaucouleurs G., de Vaucouleurs A., Corwin H. G., Jr, Buta R. J., Paturel G., Fouque P., 1991, Sky Telesc., 82, 621
Dutton A. A., van den Bosch F. C., Dekel A., 2010, MNRAS, 405, 1690
Elmegreen B. G., 1993, ApJ, 411, 170
Evans A. S., Solomon P. M., Tacconi L. J., Vavilkin T., Downes D., 2006, AJ, 132, 2398
Fanidakis N. et al., 2010, MNRAS, preprint (arXiv:1011.5222)
Faucher-Giguère C., Kereš D., 2011, MNRAS, 412, L118
Fu J., Guo Q., Kauffmann G., Krumholz M. R., 2010, MNRAS, 409, 515
Fumagalli M., Prochaska J. X., Kasen D., Dekel A., Ceverino D., Primack J. R., 2011, MNRAS, preprint (arXiv:1103.2130)
Gao Y., Solomon P. M., 2004, ApJ, 606, 271
Geach J. E., Smail I., Coppin K., Moran S. M., Edge A. C., Ellis R. S., 2009, MNRAS, 395, L62
Geach J. E., Smail I., Moran S. M., MacArthur L. A., Lagos C. d. P., Edge A. C., 2011, ApJ, 730, L19
Genzel R. et al., 2010, MNRAS, 407, 2091
Giovanelli R. et al., 2005, AJ, 130, 2598
González J. E., Lacey C. G., Baugh C. M., Frenk C. S., Benson A. J., 2009, MNRAS, 397, 1254
González J. E., Lacey C. G., Baugh C. M., Frenk C. S., 2011, MNRAS, 413, 749
Granato G. L., Lacey C. G., Silva L., Bressan A., Baugh C. M., Cole S., Frenk C. S., 2000, ApJ, 542, 710
Greve T. R. et al., 2005, MNRAS, 359, 1165
Guelin M., Zylka R., Mezger P. G., Haslam C. G. T., Kreysa E., Lemke R., Sievers A. W., 1993, A&A, 279, L37
Guimarães R., Petitjean P., de Carvalho R. R., Djorgovski S. G., Noterdaeme P., Castro S., Poppe P. C. D. R., Aghaee A., 2009, A&A, 508, 133
Haehnelt M. G., Steinmetz M., Rauch M., 1998, ApJ, 495, 647
Hughes D. H. et al., 2010, in Stepp L. M., Gilmozzi R., Hall H. J., eds, SPIE Conf. Ser. Vol. 7733, Ground-based and Airborne Telescopes III. Am. Inst. Phys., New York, p. 773312
Ivison R. J., Papadopoulos P. P., Smail I., Greve T. R., Thomson A. P., Xilouris E. M., Chapman S. C., 2011, MNRAS, 412, 1913
Johnston S. et al., 2008, Exp. Astron., 22, 151
Kennicutt R. C., Jr, 1983, ApJ, 272, 54
Kennicutt R. C., Jr, 1989, ApJ, 344, 685
Kennicutt R. C., Jr, 1998, ApJ, 498, 541
Keres D., Yun M. S., Young J. S., 2003, ApJ, 582, 659
Kim H.-S., Baugh C. M., Benson A. J., Cole S., Frenk C. S., Lacey C. G., Power C., Schneider M., 2011, MNRAS, 414, 2367
Kregel M., van der Kruit P. C., de Grijs R., 2002, MNRAS, 334, 646
Kroupa P., 2001, MNRAS, 322, 231
Krumholz M. R., McKee C. F., Tumlinson J., 2009, ApJ, 699, 850
Lacey C. G., Baugh C. M., Frenk C. S., Silva L., Granato G. L., Bressan A., 2008, MNRAS, 385, 1155
Lacey C. G., Baugh C. M., Frenk C. S., Benson A. J., 2011, MNRAS, 412, 1828
Lagos C. D. P., Cora S. A., Padilla N. D., 2008, MNRAS, 388, 587
Lagos C. D. P., Lacey C. G., Baugh C. M., Bower R. G., Benson A. J., 2011, MNRAS, 416, 1566 (L11)
Lah P. et al., 2007, MNRAS, 376, 1357
Lah P. et al., 2009, MNRAS, 399, 1447
Leroy A. K., Walter F., Brinks E., Bigiel F., de Blok W. J. G., Madore B., Thornley M. D., 2008, AJ, 136, 2782
Leroy A. K. et al., 2009, AJ, 137, 4670
Lisenfeld U. et al., 2011, A&A, preprint (arXiv:1108.2130)
McKee C. F., Ostriker E. C., 2007, ARA&A, 45, 565
Mac Low M., Klessen R. S., 2004, Rev. Mod. Phys., 76, 125
Martin A. M., Papastergis E., Giovanelli R., Haynes M. P., Springob C. M., Stierwalt S., 2010, ApJ, 723, 1359
Meier D. S., Turner J. L., 2004, AJ, 127, 2069
Meijerink R., Spaans M., Israel F. P., 2007, A&A, 461, 793
Meyer M. J. et al., 2004, MNRAS, 350, 1195
Meyer M. J., Zwaan M. A., Webster R. L., Brown M. J. I., Staveley-Smith L., 2007, ApJ, 654, 702
Narayanan D., Cox T. J., Hayward C. C., Younger J. D., Hernquist L., 2009, MNRAS, 400, 1919
Norberg P. et al., 2001, MNRAS, 328, 64
Noterdaeme P., Ledoux C., Petitjean P., Srianand R., 2008, A&A, 481, 327
Noterdaeme P., Petitjean P., Ledoux C., Srianand R., 2009, A&A, 505, 1087
Obreschkow D., Rawlings S., 2009, ApJ, 696, L129
Obreschkow D., Croton D., De Lucia G., Khochfar S., Rawlings S., 2009a, ApJ, 698, 1467
Obreschkow D., Heywood I., Klöckner H.-R., Rawlings S., 2009b, ApJ, 702, 1321
Oesch P. A. et al., 2010, ApJ, 709, L21
Okamoto T., Gao L., Theuns T., 2008, MNRAS, 390, 920
Papadopoulos P. P., 2010, ApJ, 720, 226
Parkinson H., Cole S., Helly J., 2008, MNRAS, 383, 557
Pelupessy F. I., Papadopoulos P. P., 2009, ApJ, 707, 954
Pelupessy F. I., Papadopoulos P. P., van der Werf P., 2006, ApJ, 645, 1024
Péroux C., McMahon R. G., Storrie-Lombardi L. J., Irwin M. J., 2003, MNRAS, 346, 1103
Power C., Baugh C. M., Lacey C. G., 2010, MNRAS, 406, 43
Prochaska J. X., Herbert-Fort S., Wolfe A. M., 2005, ApJ, 635, 123
Rao S. M., Turnshek D. A., Nestor D. B., 2006, ApJ, 636, 610
Rauch M., 1998, ARA&A, 36, 267
Regan M. W., Thornley M. D., Helfer T. T., Sheth K., Wong T., Vogel S. N., Blitz L., Bock D. C.-J., 2001, ApJ, 561, 218
Riechers D. A., 2011, ApJ, 730, 108
Roychowdhury S., Chengalur J. N., Begum A., Karachentsev I. D., 2009, MNRAS, 397, 1435

Saintonge A. et al., 2011, MNRAS, 415, 32
Schaye J., 2004, ApJ, 609, 667
Schaye J. et al., 2010, MNRAS, 402, 1536
Schilizzi R. T., Dewdney P. E. F., Lazio T. J. W., 2008, in Stepp L. M., Gilmozzi R., eds, SPIE Conf. Ser. Vol. 7012, Ground-based and Airborne Telescopes II. SPIE, Bellingham, p. 70121I
Schruba A., Leroy A. K., Walter F., Sandstrom K., Rosolowsky E., 2010, ApJ, 722, 1699
Scoville N. Z., Frayer D. T., Schinnerer E., Christopher M., 2003, ApJ, 585, L105
Simien F., de Vaucouleurs G., 1986, ApJ, 302, 564
Solomon P. M., Vanden Bout P. A., 2005, ARA&A, 43, 677
Solomon P. M., Downes D., Radford S. J. E., Barrett J. W., 1997, ApJ, 478, 144
Somerville R. S., Hopkins P. F., Cox T. J., Robertson B. E., Hernquist L., 2008, MNRAS, 391, 481
Spergel D. N. et al., 2003, ApJS, 148, 175
Springel V., Hernquist L., 2003, MNRAS, 339, 289
Springel V., White S. D. M., Tormen G., Kauffmann G., 2001, MNRAS, 328, 726
Springel V. et al., 2005, Nat, 435, 629
Srianand R., Gupta N., Petitjean P., Noterdaeme P., Ledoux C., 2010, MNRAS, 405, 1888
Tacconi L. J. et al., 2006, ApJ, 640, 228
Tacconi L. J. et al., 2010, Nat, 463, 781
Tecce T. E., Cora S. A., Tissera P. B., Abadi M. G., Lagos C. D. P., 2010, MNRAS, 408, 2008
Tumlinson J. et al., 2010, ApJ, 718, L156
Verheijen M. A. W., Sancisi R., 2001, A&A, 370, 765
Verheijen M., van Gorkom J. H., Szomoru A., Dwarakanath K. S., Poggianti B. M., Schiminovich D., 2007, ApJ, 668, L9
Weinzirl T., Jogee S., Khochfar S., Burkert A., Kormendy J., 2009, ApJ, 696, 411
Wong T., Blitz L., 2002, ApJ, 569, 157
Wootten A., Thompson A. R., 2009, Proc. IEEE, 97, 1463
Wyder T. K. et al., 2009, ApJ, 696, 1834
Young J. S., Knezek P. M., 1989, ApJ, 347, L55
Young J. S., Scoville N. Z., 1991, ARA&A, 29, 581
Zwaan M. A., Meyer M. J., Staveley-Smith L., Webster R. L., 2005, MNRAS, 359, L30

This paper has been typeset from a TEX/LATEX file prepared by the author.